Organic single-photon switch

Anton Zasedatelev[1] [a], Anton V. Baranikov[1], Denis Sannikov[1], Darius Urbonas[3], Fabio Scafirimuto[3], Vladislav Yu. Shishkov[4,5], Evgeny S. Andrianov[4,5], Yurii E. Lozovik[6,7], Ullrich Scherf[8], Thilo Stöferle[3], Rainer F. Mahrt[3], and Pavlos G. Lagoudakis[1,2b]

[1]*Skolkovo Institute of Science and Technology, Moscow, Russian Federation*

[2]*Department of Physics and Astronomy, University of Southampton, Southampton, SO17 1BJ, United Kingdom*

[3]*IBM Research Europe - Zurich, Säumerstrasse 4, Rüschlikon 8803, Switzerland*

[4]*Dukhov Research Institute of Automatics (VNIIA), 22 Sushchevskaya, Moscow 127055, Russia*

[5]*Moscow Institute of Physics and Technology, 9 Institutskiy per., Dolgoprudny 141700, Moscow region, Russia*

[6]*Institute for Spectroscopy RAS, 5 Fizicheskaya, Troitsk 142190, Russia*

[7]*Moscow Institute of Electronics and Mathematics, National Research University Higher School of Economics, 101000, Moscow, Russia and*

[8]*Macromolecular Chemistry Group and Institute for Polymer Technology, Bergische Universität Wuppertal, Gauss-Strasse 20, 42119 Wuppertal, Germany*

(Dated: May 12, 2021)

[a] Correspondence address: a.zasedatelev@skoltech.ru

[b] p.lagoudakis@skoltech.ru

Abstract

The recent progress in nanotechnology [1, 2] and single-molecule spectroscopy [3–5] paves the way for cost-effective organic quantum optical technologies emergent with a promise to useful devices operating at ambient conditions. We harness a π-conjugated ladder-type polymer strongly coupled to a microcavity forming hybrid light-matter states, so-called exciton-polaritons, to create exciton-polariton condensates with quantum fluid properties. Obeying Bose statistics, exciton-polaritons exhibit an extreme nonlinearity undergoing bosonic stimulation [6] which we have managed to trigger at the single-photon level, thereby providing an efficient way for all-optical ultra-fast control over the macroscopic condensate wavefunction. Here, we utilise stable excitons dressed with high energy molecular vibrations allowing for single-photon nonlinearity operation at ambient conditions. This opens new horizons for practical implementations like sub-picosecond switching, amplification and all-optical logic at the fundamental quantum limit.

Nonlinear optical phenomena are at heart of diverse applications ranging from telecommunication to data storage, high resolution microscopy, and lithography among others. In photonics, the implementation of nonlinear effects at the single photon level is highly desirable as it can drive power consumption of all-optical switches, optical modulators and optical transistors to their fundamental limit. Furthermore, single photon nonlinearities offer unique applications for optical quantum control and new paradigms for optical computing, optical communications and metrology [10, 11]. Considerable efforts are invested towards the achievement of single-photon nonlinearity across a plethora of material systems and physical principles. Platforms range from a single atom [12–15], including artificial, solid-state atoms [16–19] coupled to a high-finesse cavity probing the nonlinear regime of cavity quantum electrodynamics (cQED) to ultracold atomic ensembles [7–9]. Unlike their single emitter counterparts, the latter ones probed the single-photon nonlinearity by means of quantum interference in strongly correlated many-body systems. These systems are more robust and scalable, but sophisticated cooling and quantum-state preparation techniques, alongside with high vacuum and cryogenic conditions compromise their use significantly.

Strong coupling of semiconductor materials in optical microcavities can potentially combine the above concepts of cQED and correlated many-body physics giving rise to hybrid light-matter states that are much more robust to high temperatures [22]. Obeying Bose statistics and despite their non-equilibrium nature, under certain conditions exciton-polaritons undergo a transition to a macroscopically occupied state exhibiting off-diagonal long-range order [1, 23, 24]. The coherent and nonlinear nature of polariton condensates [27] makes them outstanding candidates for integrated on-chip photonics [6, 28, 29]. Here, we demonstrate ultra-fast single photon optical switching and amplification operational at ambient conditions, using a π-conjugated ladder-type polymer strongly coupled to an optical microcavity.

Hereafter, we employ an organic semiconductor polymer microcavity consisting of a 35 nm thick film of π-conjugated ladder-type polymer called MeLPPP, encapsulated by 50 nm SiO_2 spacers on either side sandwiched between SiO_2/Ta_2O_5 distributed Bragg reflectors (DBR) constituting a $\lambda/2$ optical microcavity (see Methods). The structure design and related properties in the strong light-matter interaction regime have been extensively studied in [1, 6, 26], and in the Supplementary Information (SI) Section I we provide further spectroscopic evidence of strong coupling. To minimise heating of the molecules, we pump

the uncoupled exciton reservoir resonantly at the exciton transition using 150 fs pulses, and optimise the incident angle of the pump beam to minimise reflection losses, as shown schematically in Fig. 1a. Exciton energy relaxation populates polariton states predominantly through intracavity radiative pumping and vibron-assisted thermalisation [4, 30, 31]. Recently, we demonstrated that in the presence of strong vibrational resonances in organic microcavities, a single step exciton-vibron scattering can efficiently populate the lower polariton dispersion [6]. Therefore, we choose the detuning of the exciton-photon resonance to satisfy the following condition: $\hbar\omega_{exc} = \hbar\omega_{pol} + \hbar\omega_{vib}$, between the exciton reservoir ($\hbar\omega_{exc}$) and the ground polariton state ($\hbar\omega_{pol}$), where $\hbar\omega_{vib}$ is the energy of the molecular vibron. By optimising the pump and detuning conditions as described above, we achieve a polariton condensation threshold at an absorbed fluence of $P_{th} \sim 8\mu J/cm^2$, i.e. $300pJ$ incident pump pulse energy (see Methods), the lowest reported across all different types of strongly coupled organic semiconductor microcavities; for comparison see Supplementary Information (SI) section II. Fig. 1b shows the pump fluence dependence of the emission intensity from the ground polariton state, where a superlinear increase above threshold is observed, indicating the transition to polariton condensation. We corroborated the transition to a polariton condensate through a full analysis of the redistribution of polaritons along the lower polariton dispersion, which exhibit a collapse of the polariton wavefunction at the ground polariton state, and a concomitant narrowing of the spectral linewidth and energy blueshift at threshold pump fluence (see SI section II).

In the following, we utilise the effectiveness of the exciton-vibron relaxation process that underpins the record-low polariton condensation threshold reported here, to trigger bosonic stimulation and amplify a seed pulse resonant to the ground polariton state, as shown in Fig. 1a (see Methods). To maximise the efficiency of stimulation towards the ground polariton state we optimise both the spatial and temporal overlap between the seed and pump beams. Finally, we attenuate the seed down to the level of $460aJ$ per pulse corresponding to ~ 1140 polaritons resonantly injected directly into the ground state. Seeding the ground polariton state drastically increases the exciton-to-polariton relaxation rate allowing for polariton condensation at half the exciton reservoir density and boosting the states occupancy. According to the pump fluence dependence presented in Fig. 1b, resonant seeding results in ~ 50 times higher integrated emission compared to the spontaneously formed condensate. The stimulation effect on energy–momentum *(E,k)* distributions of the condensate is shown

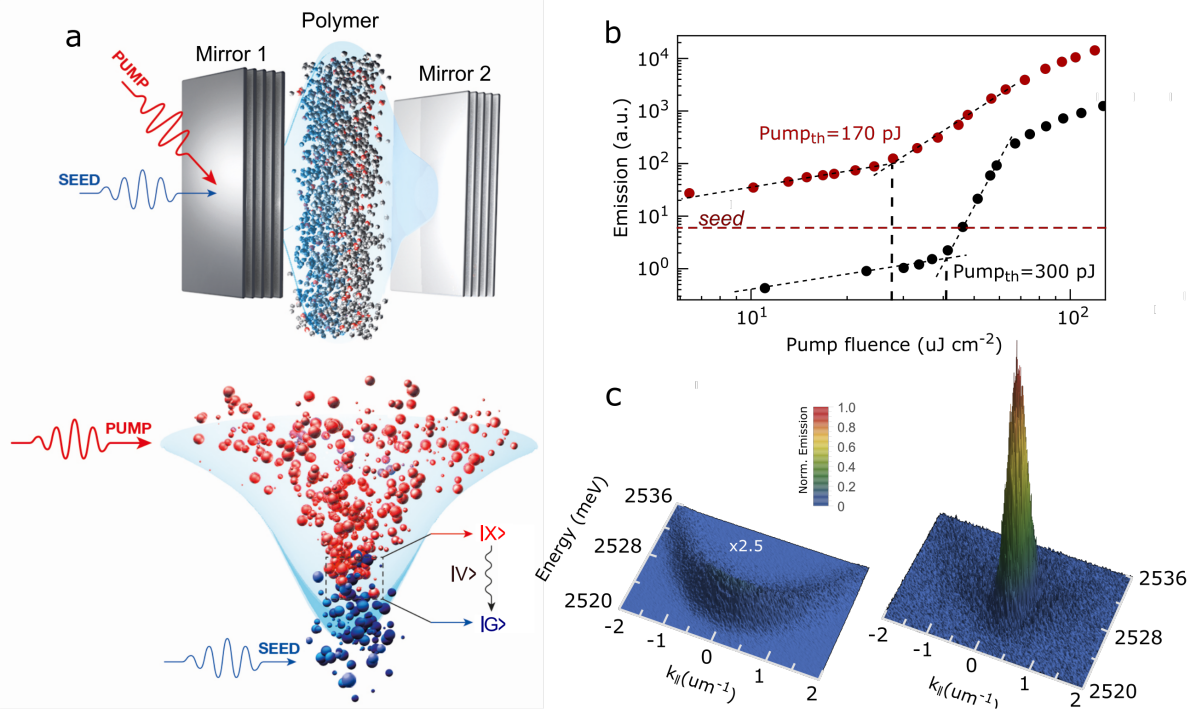

FIG. 1. **The principle of the extreme nonlinearity in organics. a**, The schematic illustrates the principle of stimulated relaxation from the exciton reservoir (X) towards the ground polariton state (G) via molecular vibron (V). **b**, Integrated emission as a function of pump fluence plotted for the spontaneously formed (black dots) and seeded (red dots) polariton condensates at a pump energy threshold of $300pJ$ and $170pJ$ respectively, shown by vertical dashed lines. **c**, Energy, momentum *(E,k)* distribution for spontaneously formed (left) and seeded (right) polariton condensates respectively. Incident pump fluence is 80 $\mu J/cm^2$ ($P \sim 2P_{th}$), energy of the seed beam is $460aJ$.

in Fig. 1c (see Methods).

Further on, we investigate the control over the condensate occupancy by harnessing progressively smaller seed energy as shown in Fig. 2a-c, respectively. With decreasing seed energy we observe a substantial reduction of the ground state population, although even at the lowest seed energy of $1aJ$, carrying on average only 2.5 photons per pulse, we are still able to resolve an increase in the condensate population. Figure 2d shows emission spectra obtained from integrated *E,k* distributions over a momentum range of ± 0.2 μm^{-1}, exhibiting a clear photoluminescence increase of the seeded (colored lines) vs spontaneously formed condensates (black line). Comparing the spectral area in Fig. 2d we detect nearly 55% difference in the ground state population for the case of $1aJ$ seed energy. To minimize fluctuations

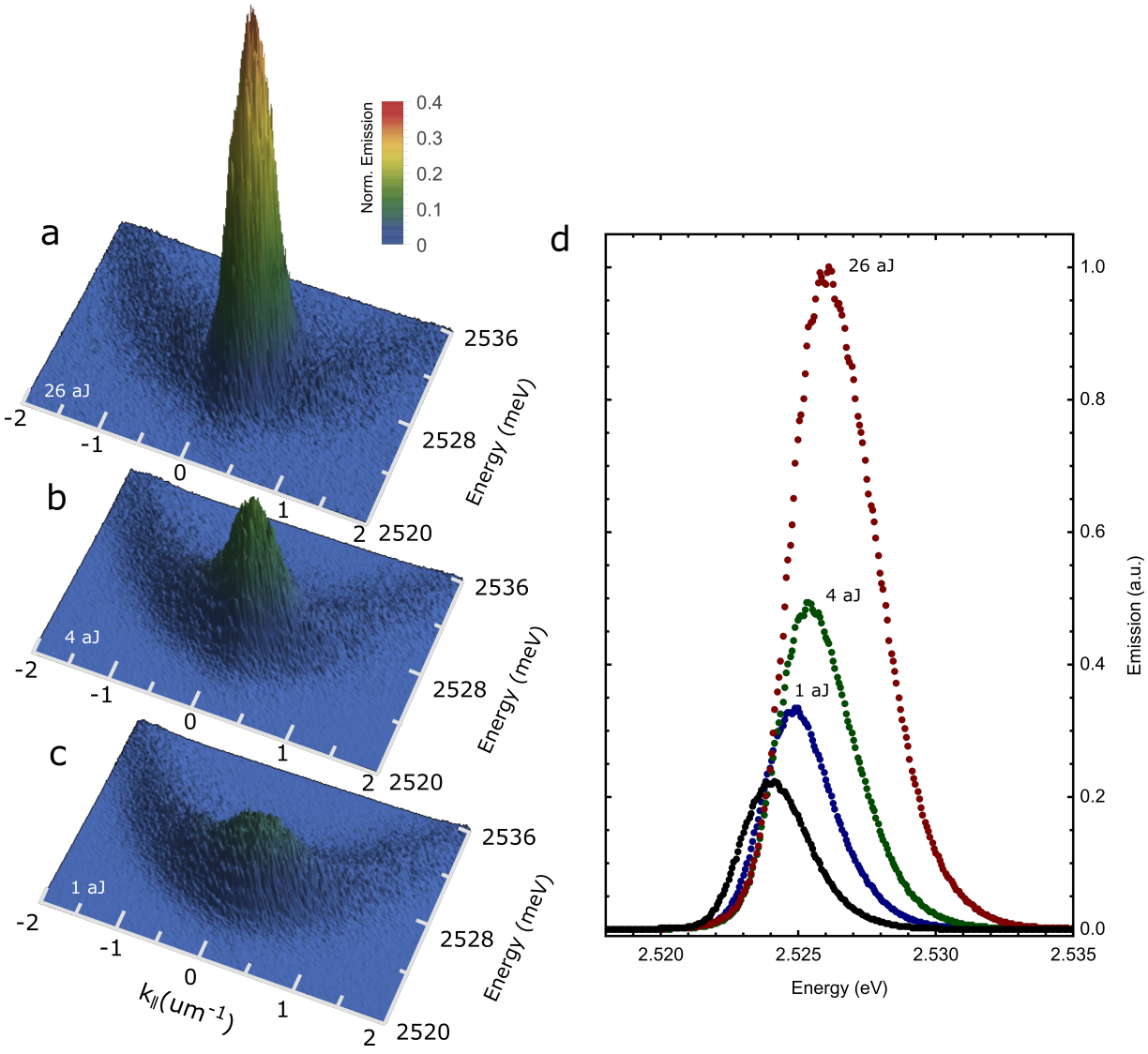

FIG. 2. **Atto-Joule polariton switch. a,b,c**, Energy, momentum *(E,k)* distributions of 5000 integrated condensate realizations, seeded with $26aJ$, $4aJ$ and $1aJ$ pulses respectively. **d**, Emission spectra obtained from *(E,k)* distributions **a-c** by integrating over ± 0.2 μm^{-1} in momentum space. Red, green and blue dots correspond to the polariton condensate seeded with $26aJ$, $4aJ$ and $1aJ$ pulses respectively, while black dots display the emission spectrum of spontaneously formed polariton condensates without seed.

of the condensate occupation number caused by the pump-induced exciton reservoir density variations, we excite the system close to the gain saturation regime at $2P_{th}$ and integrate the output signal over 5000 single-shot condensate realizations on the detector (see Methods).

We quantify the increase in the condensate occupancy on the average number of photons

in the seed pulse by defining the contrast as a figure of merit parameter depending on the ratio of integrated population at the ground state between spontaneously formed (P_{spont}) and seeded polariton condensates (P_{seed}): $Contrast = \frac{P_{seed}}{P_{spont}} - 1$. This contrast reveals a nearly power-law dependence on the average photon number of the seed, shown in Fig. 3. We experimentally observe the onset of condensation triggered by seed pulses carrying ~ 1.5 photons on average, with a probability larger than 0.95. Figure 3 shows that for the lowest energy seed pulses, the 2σ error bar clearly exceeds the 0% contrast level of spontaneously formed condensates. To describe the switching process we have developed a multi-mode microscopic theory of the seeded vibron-mediated polariton condensation (see Methods and SI section III for further details). Numerical simulations are in a good agreement with the experimentally observed contrast dependence, as shown in Fig. 3 (solid curve), integrated over ± 0.2 μm^{-1} in momentum-space. Notably, the microscopic theory predicts a contrast of $\sim 11\%$ at the single-photon level; an in-depth analysis of the mechanisms underpinning the observed nonlinearity is presented in sections IV and V of the SI.

Despite the agreement between our experimental observation and the microscopic theory, when approaching the single photon regime with a light source that obeys a Poissonian photon number distribution, the statistical properties of the source can no longer be neglected. In the few-photon regime, the tail of the distribution containing higher photon number-states can significantly contribute to polariton stimulation; the probability of having n photons in the distribution scales with its maximum at $\langle n \rangle$ average photons as $\frac{\langle n \rangle !}{n!} \langle n \rangle^{n-\langle n \rangle}$. For example, for a seed pulse with four photons on average instances of 10-photon events occur with ~ 37 times lower probability than 4-photon events. Therefore, at the few-photon regime, integrated measurements of the photoluminescence intensity over thousands of seed pulses, may be skewed by higher photon number states.

To address this conundrum, we implement a single-shot measurement technique, using the same pump-seed excitation geometry, whilst allowing for pulse-to-pulse analysis of the condensate population, and record the photoluminescence in real-space, using appropriate filtering in momentum-space (within $\pm 1 \mu$m^{-1}, see Methods). We seed the ground-state for 300 sequentially recorded pulses, and then we switch the seed beam off allowing for 300 successive realizations of spontaneously-formed polariton condensates and repeat the whole sequence three consecutive times as shown in Fig. 4a-e. Single-shot condensate realisations, in the presence/absence of seed pulses containing $\langle n \rangle = 600$, 60, 9.3, 2.7, and 1 photon

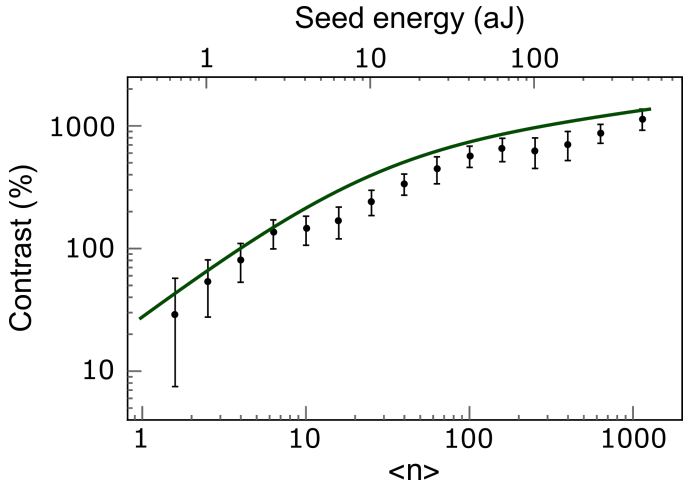

FIG. 3. **Polariton switching contrast towards the single-photon level.** The contrast in population between seeded and spontaneously formed polariton condensates as the function of seed energy (top axis) and average photon number per pulse (bottom axis). Solid curve shows the result of numerical simulations of the microscopic theoretical model. The error bars show 2σ (95.4%) confidence intervals of the switching contrast.

per pulse, reveal a contrast with an average value of about 350%, 160%, 60%, 25% and 11%, respectively. The right panels of Fig. 4a-e show histograms of the polariton population for each spontaneously-formed (black) and seeded (red) condensate realizations fitted by Gaussian distributions. The Gaussian fit is justified by a large number of polaritons in the condensate exhibiting excessive noise in the total polariton number. A relatively large noise is most likely the result of dynamic spatial disorder of the condensate [28, 29] which is transformed to the disorder in the momentum space. Shot-to-shot fluctuations of the condensate in the momentum space lead to the excessive intensity noise in our detection scheme as the momentum-filter is used. Therefore, the contrast to noise ratio in this case is not limited by any fundamental reason and, in principle, can be improved substantially by means of engineering the filter bandwidth, size of the condensate, pump fluence, configuration of seeded states etc. As the experimental distributions are well-approximated by Gaussian distributions, our statistical analysis yields almost the same mean contrast values of 360%, 160%, 63%, 26% and 11% as shown in Fig. 4f. We note that the results obtained from single-shot condensate realisations show a lower contrast at the single-photon regime, with respect to the integrated measurements of Fig. 3, i.e. 11% vs 20%, while exhibiting

the theoretically predicted power-law contrast dependence on $\langle n \rangle$ integrated over $\pm 1 \mu \mathrm{m}^{-1}$ in momentum-space.

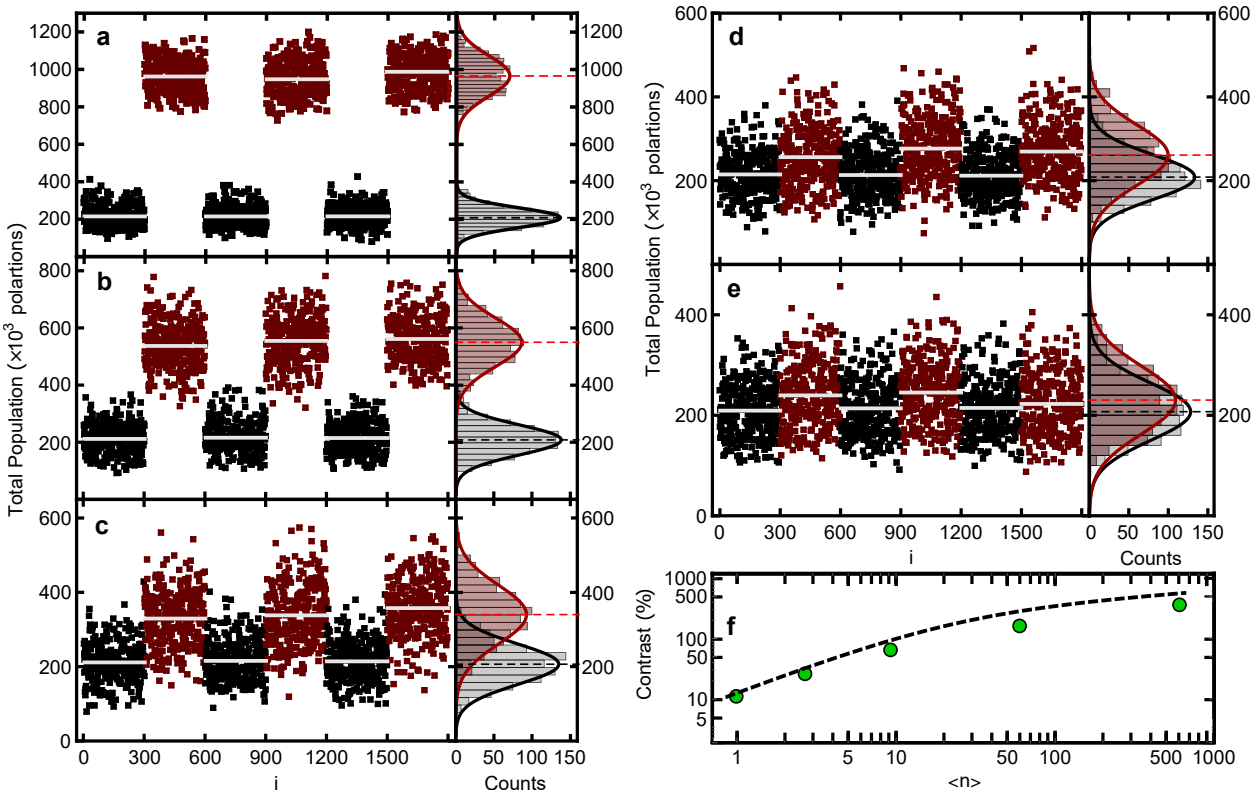

FIG. 4. **Single-photon switching for single-shot condensate realisations. a-e**, Total polariton populations recorded within $\pm 1 \mu \mathrm{m}^{-1}$ wavevector range in the single-shot regime for a sequence of 300-to-300 spontaneously formed (black dots) and seeded (red dots) polariton condensate realisations. Seeded realisations are triggered by $\langle n \rangle$ equals 600, 60, 9.3, 2.7, and 1 photon per pulse on average as shown in **a-e** respectively. Right panels represent histograms of total polariton population within single-shot condensate realisations seeded with the respective $\langle n \rangle$ photon number state (red) as well histograms of the spontaneously formed condensates (black), both fitted by Gaussian distributions. **f**, Switching contrast versus average number of photons $\langle n \rangle$ per seed pulse obtained from statistical analysis of the histograms. The dashed curve shows the result of numerical simulations of the microscopic theoretical model.

In conclusion, we report experimental evidence of single-photon nonlinearity in organic polariton condensates, underpinned by bosonic stimulation of exciton-polaritons to the ground polariton state. Our investigation demonstrates few-photon control over the polariton condensate occupancy with a record amplification of $\sim$ 23000 polaritons for every

resonantly injected polariton. At the single average photon level, we observe all-optical polariton switching with a contrast of $\sim 20\%$ as evidenced from time-integrated measurements, and $\sim 11\%$ following a pulse-to-pulse analysis of single-shot condensate realisations. The rapid progress of organic polaritonics has opened new routes for all-optical switching and logic at ambient conditions [6, 26]. Our investigation here takes these applications to the single-photon level thereby bridging quantum properties of light with classical phenomena of massively occupied states of light-matter Bose-Einstein condensates.

[1] Chikkaraddy, R. *et al.* Single-molecule strong coupling at room temperature in plasmonic nanocavities. *Nature* **535**, 128 (2016).

[2] Hail, C.U. *et al.* Nanoprinting organic molecules at the quantum level. *Nat. Commun.* **10**, 1880 (2019).

[3] Maser, A. *et al.* Few-photon coherent nonlinear optics with a single molecule. *Nat. Photon.* **10**, 450 (2016).

[4] Wang, D. *et al.* Coherent Coupling of a Single Molecule to a Scanning Fabry-Perot Microcavity. *Phys. Rev. X* **7**, 021014 (2017).

[5] Wang, D. *et al.* Turning a molecule into a coherent two-level quantum system. *Nat. Phys.* **15**, 483 (2019).

[6] Zasedatelev, A.V. *et al.* A room-temperature organic polariton transistor. *Nat. Photon.* **13**, 378 (2019).

[7] Peyronel, T. *et al.* Quantum nonlinear optics with single photons enabled by strongly interacting atoms. *Nature* **488**, 57 (2012).

[8] Chen, W. *et al.* All-Optical Switch and Transistor Gated by One Stored Photon. *Science* **341**, 768 (2013).

[9] Gorniaczyk, H. *et al.* Single-Photon Transistor Mediated by Interstate Rydberg Interactions. *Phys. Rev. Lett.* **113**, 053601 (2014).

[10] Walmsley, I.A. Quantum optics: Science and technology in a new light. *Science* **348**, 525 (2015).

[11] Chang, D.E. *et al.* Quantum nonlinear optics photon by photon. *Nat. Photon.* **6**, 685 (2014).

[12] Reiserer, A. *et al.* Nondestructive Detection of an Optical Photon. *Science* **342**, 1349 (2013).

[13] Shomroni, I. *et al.* All-optical routing of single photons by a one-atom switch controlled by a single photon. *Science* **346**, 903 (2014).

[14] Tiecke, T.G. *et al.* Nanophotonic quantum phase switch with a single atom. *Nature* **508**, 241 (2014).

[15] Hacker, B. *et al.* A photon-photon quantum gate based on a single atom in an optical resonator. *Nature* **536**, 193 (2016).

[16] Volz, T. *et al.* Ultrafast all-optical switching by single photons. *Nat. Photon.* **6**, 605 (2012).

[17] Giesz, V. *et al.* Coherent manipulation of a solid-state artificial atom with few photons. *Nat. Commun.* **7**, 11986 (2016).

[18] Sun, S. *et al.* A single-photon switch and transistor enabled by a solid-state quantum memory. *Science* **361**, 57 (2018).

[19] Dietrich, C.P. *et al.* GaAs integrated quantum photonics: Towards compact and multi-functional quantum photonic integrated circuits. *Laser Photonics Rev.* **10**, 870 (2016).

[20] Ojambati, O.S. *et al.* Quantum electrodynamics at room temperature coupling a single vibrating molecule with a plasmonic nanocavity. *Nat. Commun.* **10**, 1049 (2019).

[21] Liu, R. *et al.* Strong Light-Matter Interactions in Single Open Plasmonic Nanocavities at the Quantum Optics Limit. *Phys. Rev. Lett.* **118**, 237401 (2017).

[22] Sanvitto, D., Kéna-Cohen, S., The road towards polaritonic devices. *Nat. Mater.* **15**, 1061 (2016).

[23] Deng, H., Haug, H., Yamamoto, Y. Exciton-polariton Bose-Einstein condensation. *Rev. Mod. Phys.* **82**, 1489 (2010).

[24] Kasprzak, J. *et al.* Bose–Einstein condensation of exciton polaritons. *Nature* **443**, 409-414 (2006).

[25] Plumhof, J. D., Stöferle, T. Mai, L., Scherf, U. & Mahrt, R. F. Room-temperature bose-einstein condensation of cavity exciton-polaritons in a polymer. *Nat. Mater.* **13**, 247-252 (2014).

[26] Baranikov, A. V., *et al.* All-optical cascadable universal logic gate with sub-picosecond operation. *arXiv:2005.04802* (2020).

[27] Carusotto, I., Ciuti, C. Quantum fluids of light. *Rev. Mod. Phys.* **85**, 299 (2013).

[28] Lerario, G. *et al.* Room-temperature superfluidity in a polariton condensate. *Nat. Phys.* **13**, 837-841 (2017).

[29] Sun, Z., Snoke, D.W. Optical switching with organics. *Nat. Photon.* **13**, 370 (2019).

[30] Tartakovskii, A.I. *et al.* Raman scattering in strongly coupled organic semiconductor microcavities. *Phys. Rev. B* **63**, 121302 (2001).

[31] Coles, D. M. *et al.* Vibrationally assisted polariton-relaxation processes in strongly coupled organic-semiconductor microcavities. *Adv. Funct. Mater.* **21**, 3691–3696 (2011).

[32] Grant, R.T. *et al.* Efficient Radiative Pumping of Polaritons in a Strongly Coupled Microcavity by a Fluorescent Molecular Dye. *Adv. Opt. Mater.* **4**, 1615 (2016).

[33] Daskalakis, K.S., Maier, S.A. & Kéna-Cohen, S. Spatial Coherence and Stability in a Disordered Organic Polariton Condensate. *Phys. Rev. Lett.* **115**, 035301 (2015).

[34] Bobrovska, N. *et al.* Dynamical Instability of a Nonequilibrium Exciton-Polariton Condensate. *ACS Photon.* **5**, 111 (2018).

METHODS

Sample fabrication.

The sample is composed of a bottom distributed Bragg reflector (DBR) on a fused silica substrate - mirror 2, a central cavity defect region with an effective thickness slightly larger than half the exciton transition wavelength, and a top DBR - mirror 1. The DBRs consist of alternating SiO_2/Ta_2O_5 quarter-wavelength-thick layers produced by sputter deposition (9+0.5 pairs for the bottom DBR, 6+0.5 for the top DBR). The center of the cavity consists of the polymer layer sandwiched between 50-nm spacer layers of sputtered SiO_2. The SiO_2 spacer is sputtered on the organic using a SiO_2 sputter target. Methyl-substituted ladder-type poly(p-phenylene) (MeLPPP; $M_n = 31500$, $M_w = 79000$) was synthesized as described elsewhere [35]. MeLPPP is dissolved in toluene and spin-coated on the bottom spacer layer. The film thickness of approximately 35 nm is measured with a profilometer (Veeco Dektak).

Spectroscopy. The pump beam with 150-200 fs pulse duration was generated by a tunable optical parametric amplifier (Coherent OPerA SOLO) which was pumped by 500 Hz high energy Ti:Sapphire regenerative amplifier (Coherent Libra-HE). The center wavelength was adjusted with respect to experiments at 2.72 eV having 30 meV full-width at half-maximum (FWHM). The angle of incidence to the sample was 45°. The pulses were focused at the sample to a 20 μm $\times 32\ \mu m$ Gaussian spot at full width at half maximum. We measured the reflectance of the beam at 45 degree of incidence (R=0.81). Since the transmitted light through the sample is negligible and strongly dependent on scattering from defects, we assumed that it is all absorbed by the structure (1-R=0.19), thus providing an upper boundary of the absorbed fluence. Therefore, the given incident fluence of 42 J/cm2 at the threshold of the spontaneously formed condensate becomes 8 J/cm2 in terms of the absorbed value.

Filtered broadband white-light-continuum (WLC) generated in a sapphire plate with photon energies in the range 2.45 - 2.6 eV was utilized as the seed beam having 150-250 fs pulse duration. The seed beam was focused on the sample at the normal incidence to 5 μm spot size with a micro-objective (10x Nikon, 0.3 NA) which allows to seed the ground polariton state within a wavevector range of $\pm 0.2\mu m^{-1}$. The energy of the seed beam is defined as the incident pulse within the full linewidth of the seeded state (i.e. before sample). In all measurements, temporal and spatial overlap between the control and the pump beams

were optimized by maximizing the signal of the output nonlinear emission from the sample. Temporal overlap was varied by using a motorized translation stage with retroreflector in the seed beam optical path.

Integrated energy-momentum *E,k* distributions were acquired in transmission geometry. Output emission of the sample was collected with a 10X Mitutoyo plan apo infinity corrected objective (NA = 0.28) and coupled to a 750 mm spectrometer (Princeton Instruments SP2750) equipped with an electron multiplying CCD camera (Princeton Instruments ProEM 1024BX3). The emission was spectrally and in-plane wavevector resolved using a 1200 grooves/mm grating and a slit width of 50 μm at the entrance of the spectrometer. To obtain the incident excitation density of the pump pulse, the average pump power was measured using a calibrated Si photodetector (Thorlabs-Det10/M) and an oscilloscope (Keysight DSOX3054T) for data acquisition. Accuracy verification of the power measurements was carried out by using two independent power meters: 1 - Si photodiode power sensor (Thorlabs-S120VC) with a power meter console (Thorlabs-PM100D), 2 - thermal power sensor (Thorlabs-S302C) equipped with the power meter console (Thorlabs-PM100D). The energy of the seed beam was calibrated by using standard power meter measurements and additionally verified through a single photon counting technique using a photon counting module (SPC-160, Becker & Hickl GmbH) and a single-photon avalanche Si photodiode (IDQ 100), for details see Fig. S5 in Section VII of SI. All the measurements for Fig. 2 and 3 are carried out under the same incident pump fluence of $P_{pump} = 80\mu Jcm^{-2}$ ($P \sim 2P_{th}$) to minimize the noise level originating from pump power fluctuations and high nonlinearity of the sample above the threshold. Pump fluence dependencies in Fig. 1b as well as spectra in Fig. 2d and the contrast dependence in Fig. 3 are plotted for the ground polariton state integrated within $\pm 0.2\mu\mathrm{m}^{-1}$.

Polariton single-condensate realizations were investigated by means of a single-shot real space imaging technique using the same pump conditions ($P \sim 2P_{th}$) with individual pulse control. The images were recorded by means of an electron multiplying CCD camera applying 100x EM gain and operating in a single frame acquisition mode. To reduce the contribution of non-condensed polariton density we filtered out the output emission above $\pm 1\mu\mathrm{m}^{-1}$ in Fourier space. To reduce the noise originated from pump fluctuation we recorded only realizations which obey 2% of tolerance interval in incident pump energy. The energy of incident pump pulses for each condensate realisation was recorded using a calibrated photodetector

and an oscilloscope. Using this selection criterion we recorded the single-condensate realisations represented in Fig. 4a-e by seeding the ground state for 300 sequential pulses followed by seed beam off measurements that allow for 300 realizations of spontaneously-built polariton condensates. The whole sequence was repeated three times for each seed pulse energy. The incident seed energy was stabilised at the level of 2% standard deviation. Statistical analysis and calculation of the single-realisation contrast in Fig. 4a-e were carried out through processing of all 900 spontaneously built and 900 seeded condensate realisations for each seed energy.

Theoretical model.

The system is treated microscopically by considering a thin organic active layer (MeLPPP) placed in the cavity excited by an external wave that corresponds to the pump beam. The pump wave induces the dipole moment transition of organics creating Frenkel-type excitons. In turn, the excitons interact with both vibrons and cavity modes. Hereby we consider the pump exciting organic layer resonantly to the exciton transition. The Hamiltonian of the whole system has the following form:

$$\hat{H} = \hat{H}_{\text{cav}} + \hat{H}_{\text{exc}} + \hat{H}_{\text{vib}} + \hat{H}_{\text{exc-cav}} + \hat{H}_{\text{exc-vib}} \tag{1}$$

where the terms correspond to uncoupled cavity modes, excitons, vibrons, interactions between excitons and cavity modes, excitons and vibrons listed as they appear in Eq. (1). For further details see section II in SI. On the next step we make a transformation from treating the system in form of uncoupled excitons and cavity modes to their hybridized solutions: exciton-polaritons. We diagonalize the corresponding part of the full Hamiltonian, namely $\hat{H}_{\text{cav}} + \hat{H}_{\text{exc}} + \hat{H}_{\text{exc-cav}}$, and introduce operators for the lower polaritons $\hat{s}_{\text{low}\mathbf{k}}$ and upper polaritons $\hat{s}_{\text{up}\mathbf{k}}$ using the transformation below:

$$\hat{s}_{\text{up}\mathbf{k}} = \hat{c}_{\text{exc}\mathbf{k}} \cos\varphi_{\mathbf{k}} + \hat{a}_{\text{cav}\mathbf{k}} \sin\varphi_{\mathbf{k}} \tag{2}$$

$$\hat{s}_{\text{low}\mathbf{k}} = \hat{a}_{\text{cav}\mathbf{k}} \cos\varphi_{\mathbf{k}} - \hat{c}_{\text{exc}\mathbf{k}} \sin\varphi_{\mathbf{k}} \tag{3}$$

where $\hat{a}_{\text{cav}\mathbf{k}}$ and $\hat{c}_{\text{exc}\mathbf{k}}$ are cavity photon and exciton operators respectively, and

$$\varphi_{\mathbf{k}} = \frac{1}{2}\text{arctg}\left(\frac{2\Omega_{\text{R}\mathbf{k}}}{\omega_{\text{exc}} - \omega_{\text{cav}\mathbf{k}}}\right) \tag{4}$$

with $\Omega_{\text{R}\mathbf{k}} = \sqrt{N_{\text{mol}}}\Omega_{1\text{R}\mathbf{k}}$ - the Rabi frequency of exciton-photon interaction for the excitons and the cavity mode with $\hbar\mathbf{k}$ in-plane momentum.

Following the transformations above the full Hamiltonian (1) takes the form

$$\begin{aligned}\hat{H} = &\sum_{\mathbf{k}} \hbar\omega_{\text{up}\mathbf{k}} \hat{s}^{\dagger}_{\text{up}\mathbf{k}} \hat{s}_{\text{up}\mathbf{k}} + \sum_{\mathbf{k}} \hbar\omega_{\text{low}\mathbf{k}} \hat{s}^{\dagger}_{\text{low}\mathbf{k}} \hat{s}_{\text{low}\mathbf{k}} + \sum_{\mathbf{q}} \hbar\omega_{\text{vib}} \hat{b}^{\dagger}_{\mathbf{q}} \hat{b}_{\mathbf{q}} + \\ &+ \sum_{\mathbf{k}} \sum_{\mathbf{k}'} \hbar g \left(\hat{s}^{\dagger}_{\text{up}\mathbf{k}} \cos\varphi_{\mathbf{k}} - \hat{s}^{\dagger}_{\text{low}\mathbf{k}} \sin\varphi_{\mathbf{k}}\right) \left(\hat{s}_{\text{up}\mathbf{k}'} \cos\varphi_{\mathbf{k}'} - \hat{s}_{\text{low}\mathbf{k}'} \sin\varphi_{\mathbf{k}'}\right) \left(\hat{b}^{\dagger}_{-(\mathbf{k}-\mathbf{k}')} + \hat{b}_{\mathbf{k}-\mathbf{k}'}\right)\end{aligned} \tag{5}$$

The polaritons and vibrons interact with the environment that in turn initiates relaxation processes. We describe the relaxation processes within the formalism of Lindblad superoperators for a density matrix $\hat{\rho}$ of both polaritons and vibrons. The Lindblad superoperators for the lower, upper polaritons and vibrons, respectively, have the form

$$\hat{L}_{\mathrm{low}}\left(\hat{\rho}\right)=\sum_{\mathbf{k}}\frac{\gamma_{\mathrm{low}\mathbf{k}}}{2}\left(2\hat{s}_{\mathrm{low}\mathbf{k}}\hat{\rho}\hat{s}_{\mathrm{low}\mathbf{k}}^{\dagger}-\hat{s}_{\mathrm{low}\mathbf{k}}^{\dagger}\hat{s}_{\mathrm{low}\mathbf{k}}\hat{\rho}-\hat{\rho}\hat{s}_{\mathrm{low}\mathbf{k}}^{\dagger}\hat{s}_{\mathrm{low}\mathbf{k}}\right) \tag{6}$$

$$\hat{L}_{\mathrm{up}}\left(\hat{\rho}\right)=\sum_{\mathbf{k}}\frac{\gamma_{\mathrm{up}\mathbf{k}}}{2}\left(2\hat{s}_{\mathrm{up}\mathbf{k}}\hat{\rho}\hat{s}_{\mathrm{up}\mathbf{k}}^{\dagger}-\hat{s}_{\mathrm{up}\mathbf{k}}^{\dagger}\hat{s}_{\mathrm{up}\mathbf{k}}\hat{\rho}-\hat{\rho}\hat{s}_{\mathrm{up}\mathbf{k}}^{\dagger}\hat{s}_{\mathrm{up}\mathbf{k}}\right) \tag{7}$$

$$\hat{L}_{\mathrm{vib}}\left(\hat{\rho}\right)=\sum_{\mathbf{q}}\frac{\gamma_{\mathrm{vib}}}{2}\left(1+n_{\mathrm{vib}}^{\mathrm{th}}\right)\left(2\hat{b}_{\mathbf{q}}\hat{\rho}\hat{b}_{\mathbf{q}}^{\dagger}-\hat{b}_{\mathbf{q}}^{\dagger}\hat{b}_{\mathbf{q}}\hat{\rho}-\hat{\rho}\hat{b}_{\mathbf{q}}^{\dagger}\hat{b}_{\mathbf{q}}\right)+\sum_{\mathbf{q}}\frac{\gamma_{\mathrm{vib}}}{2}n_{\mathrm{vib}}^{\mathrm{th}}\left(2\hat{b}_{\mathbf{q}}^{\dagger}\hat{\rho}\hat{b}_{\mathbf{q}}-\hat{b}_{\mathbf{q}}\hat{b}_{\mathbf{q}}^{\dagger}\hat{\rho}-\hat{\rho}\hat{b}_{\mathbf{q}}\hat{b}_{\mathbf{q}}^{\dagger}\right) \tag{8}$$

where $\gamma_{\mathrm{low}\mathbf{k}}$, $\gamma_{\mathrm{up}\mathbf{k}}$ and γ_{vib} are the dissipation rates of lower, upper polaritons and the vibrons respectively, and $n_{\mathrm{vib}}^{\mathrm{th}}=1/(\exp\left(\hbar\omega_{\mathrm{vib}}/k_{\mathrm{B}}T\right)-1)$ is the thermal distribution of vibrons at an effective MeLPPP temperature T and k_{B} is the Boltzmann constant.

Thermalization of the lower polaritons is described by the following Lindblad term:

$$\hat{L}_{\mathrm{th}}\left(\hat{\rho}\right)=\sum_{\mathbf{k}_1,\mathbf{k}_2}\frac{\gamma_{\mathrm{low}}^{\mathbf{k}_1\mathbf{k}_2}}{2}\left(2\hat{s}_{\mathrm{low}\mathbf{k}_2}\hat{s}_{\mathrm{low}\mathbf{k}_1}^{\dagger}\hat{\rho}\hat{s}_{\mathrm{low}\mathbf{k}_1}\hat{s}_{\mathrm{low}\mathbf{k}_2}^{\dagger}-\hat{s}_{\mathrm{low}\mathbf{k}_1}\hat{s}_{\mathrm{low}\mathbf{k}_2}^{\dagger}\hat{s}_{\mathrm{low}\mathbf{k}_2}\hat{s}_{\mathrm{low}\mathbf{k}_1}^{\dagger}\hat{\rho}-\hat{\rho}\hat{s}_{\mathrm{low}\mathbf{k}_1}\hat{s}_{\mathrm{low}\mathbf{k}_2}^{\dagger}\hat{s}_{\mathrm{low}\mathbf{k}_2}\hat{s}_{\mathrm{low}\mathbf{k}_1}^{\dagger}\right) \tag{9}$$

Here $\gamma_{\mathrm{low}}^{\mathbf{k}_1\mathbf{k}_2}$ is the rate of energy flow from the lower polaritons having in-plane wavevector $\mathbf{k}_2$ towards ones with wavevector $\mathbf{k}_1$. According to Kubo-Martin-Schwinger relation, the rate $\gamma_{\mathrm{low}}^{\mathbf{k}_1\mathbf{k}_2}$ satisfies

$$\gamma_{\mathrm{low}}^{\mathbf{k}_1\mathbf{k}_2}=\gamma_{\mathrm{low}}^{\mathbf{k}_2\mathbf{k}_1}\exp\left(\frac{\hbar\omega_{\mathrm{low}\mathbf{k}_2}-\hbar\omega_{\mathrm{low}\mathbf{k}_1}}{k_{\mathrm{B}}T}\right) \tag{10}$$

where T is the environment temperature.

The incoherent pump of the lower and upper polaritons is described by the Lindblad

superoperator:

$$\hat{L}_{\text{pump}}(\hat{\rho}) = \sum_{\mathbf{k}} \frac{\kappa_{\text{low}\mathbf{k}}(t)}{2}\left(2\hat{s}_{\text{low}\mathbf{k}}\hat{\rho}\hat{s}^{\dagger}_{\text{low}\mathbf{k}} - \hat{s}^{\dagger}_{\text{low}\mathbf{k}}\hat{s}_{\text{low}\mathbf{k}}\hat{\rho} - \hat{\rho}\hat{s}^{\dagger}_{\text{low}\mathbf{k}}\hat{s}_{\text{low}\mathbf{k}}\right) + \sum_{\mathbf{k}} \frac{\kappa_{\text{low}\mathbf{k}}(t)}{2}\left(2\hat{s}^{\dagger}_{\text{low}\mathbf{k}}\hat{\rho}\hat{s}_{\text{low}\mathbf{k}} - \hat{s}_{\text{low}\mathbf{k}}\hat{s}^{\dagger}_{\text{low}\mathbf{k}}\hat{\rho} - \hat{\rho}\hat{s}_{\text{low}\mathbf{k}}\hat{s}^{\dagger}_{\text{low}\mathbf{k}}\right) + \sum_{\mathbf{k}} \frac{\kappa_{\text{up}\mathbf{k}}(t)}{2}\left(2\hat{s}_{\text{up}\mathbf{k}}\hat{\rho}\hat{s}^{\dagger}_{\text{up}\mathbf{k}} - \hat{s}^{\dagger}_{\text{up}\mathbf{k}}\hat{s}_{\text{up}\mathbf{k}}\hat{\rho} - \hat{\rho}\hat{s}^{\dagger}_{\text{up}\mathbf{k}}\hat{s}_{\text{up}\mathbf{k}}\right) + \sum_{\mathbf{k}} \frac{\kappa_{\text{up}\mathbf{k}}(t)}{2}\left(2\hat{s}^{\dagger}_{\text{up}\mathbf{k}}\hat{\rho}\hat{s}_{\text{up}\mathbf{k}} - \hat{s}_{\text{up}\mathbf{k}}\hat{s}^{\dagger}_{\text{up}\mathbf{k}}\hat{\rho} - \hat{\rho}\hat{s}_{\text{up}\mathbf{k}}\hat{s}^{\dagger}_{\text{up}\mathbf{k}}\right) \quad (11)$$

The seed to the lower polaritons is described by the Lindblad superoperator:

$$\hat{L}_{\text{seed}}(\hat{\rho}) = \sum_{\mathbf{k}} \frac{\kappa_{\text{seed}\mathbf{k}}(t)}{2}\left(2\hat{s}_{\text{low}\mathbf{k}}\hat{\rho}\hat{s}^{\dagger}_{\text{low}\mathbf{k}} - \hat{s}^{\dagger}_{\text{low}\mathbf{k}}\hat{s}_{\text{low}\mathbf{k}}\hat{\rho} - \hat{\rho}\hat{s}^{\dagger}_{\text{low}\mathbf{k}}\hat{s}_{\text{low}\mathbf{k}}\right) + \sum_{\mathbf{k}} \frac{\kappa_{\text{seed}\mathbf{k}}(t)}{2}\left(2\hat{s}^{\dagger}_{\text{low}\mathbf{k}}\hat{\rho}\hat{s}_{\text{low}\mathbf{k}} - \hat{s}_{\text{low}\mathbf{k}}\hat{s}^{\dagger}_{\text{low}\mathbf{k}}\hat{\rho} - \hat{\rho}\hat{s}_{\text{low}\mathbf{k}}\hat{s}^{\dagger}_{\text{low}\mathbf{k}}\right) \quad (12)$$

Finally, we use a standard Lindblad master equations including the full Hamiltonian (5) and the Lindblad terms (6-9) described above:

$$\frac{d\hat{\rho}}{dt} = \frac{i}{\hbar}\left[\hat{\rho}, \hat{H}\right] + \hat{L}_{\text{up}}(\hat{\rho}) + \hat{L}_{\text{low}}(\hat{\rho}) + \hat{L}_{\text{vib}}(\hat{\rho}) + \hat{L}_{\text{th}}(\hat{\rho}) + L_{\text{pump}}(\hat{\rho}) + L_{\text{seed}}(\hat{\rho}) \quad (13)$$

For further details see sections III and IV in SI.

---

[35] Scherf, U., Bohnen, A. & Müllen, K. Polyarylenes and poly (arylenevinylene) s, 9 The oxidized states of a (1, 4-phenylene) ladder polymer. *Makromol. Chem.* **193**, 1127–1133 (1992).

DATA AVAILABILITY

All data supporting this study are openly available from the University of Southampton repository at https://doi.org/10.5258/SOTON/D1374.

ACKNOWLEDGEMENTS

This work was supported by the Russian Scientific Foundation (RSF) grant No. 20-72-10145 and the UKs Engineering and Physical Sciences Research Council grant EP/M025330/1 to P.G.L on Hybrid Polaritonics and the RFBR according to the research projects No. 20-52-12026 (jointly with DFG) and No. 20-02-00919. E.S.A. and V.Yu.Sh. thank the Foundation for the Advancement of Theoretical Physics and Mathematics Basis. Yu.E.L. acknowledges support by Program of Basic Research of the National Research University Higher School of Economics. D.U., F.S. and T.S. acknowledge support by QuantERA project RouTe (SNSF Grant No. 20QT21_175389). P.G.L, D.U., T.S. and R.F.M. acknowledge support by European H2020-FETOPEN project POLLOC (Grant No. 899141).

AUTHOR CONTRIBUTIONS

A.Z., A.V.B. and D.S. performed the experiments and analysed the data. D.U., F.S., T.S., and R.F.M. contributed to the design and fabrication of the organic microcavity. U.S. synthesised the organic material. V.Yu.Sh., E.S.A. and Yu.E.L. developed microscopic theory and carried out numerical simulations. A.Z. and P.G.L. designed and led the research. The manuscript was written through contributions from all authors. All authors have given approval to the final version of the manuscript.

ADDITIONAL INFORMATION

The authors declare no competing financial interests.

Supplementary Information: Organic single-photon switch

I. STRONGLY COUPLED EXCITON-POLARITON SYSTEM

Although strong coupling in the microcavity sample used in this study was reported previously [1, 2], in this section we provide further experimental evidence of strong coupling. With reference to the experimental configuration for the demonstration of strong coupling here, our organic microcavity consists of a conjugated methyl-substituted ladder-type poly(-para-phenylene) (MeLPPP) polymer that has a relatively rigid backbone due to a methylene bridge between phenyl rings (inset of Fig. S1 shows the chemical structure) and, thus, exhibits pronounced singlet-related optical transitions and a high photoluminescence quantum yield. Fig. S1 shows an absorption and photoluminescence spectra of a spin-cast MeLPPP film with 35 nm thickness on fused silica, corrected for reflection of the substrate.

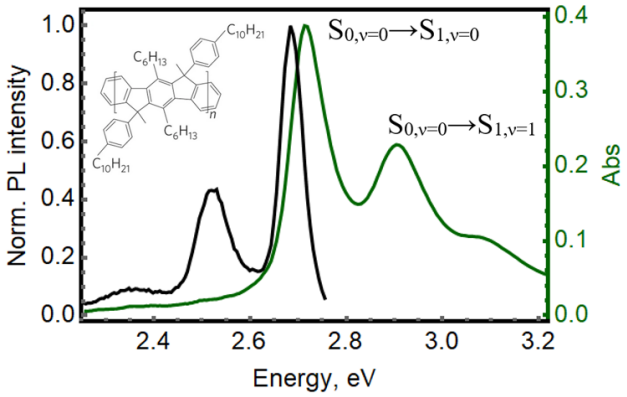

FIG. S1. Absorption (green) and photoluminescence (black) spectra of a spin-cast MeLPPP film with 35 nm thickness on fused silica, corrected for reflection of the substrate, Inset: chemical structure of the MeLPPP polymer.

Strong light-matter interaction of the polymer film with the cavity mode leads to new eigenstates of the system, namely lower, middle and upper polariton branches, following the coupling of both sub-levels of the first excited singlet state of MeLPPP. All three polariton branches can be accessed experimentally through angle dependent reflectivity measurements as was demonstrated experimentally in our previous studies [1, 2] with the typical normal mode splitting in the range of 120-140 meV (vacuum Rabi splitting). In this study we use the same sample, the only difference is the cavity photon - exciton detuning, we choose one

that corresponds to the ground polariton state energy of 2.52 eV. In this regime we benefit from the highest efficiency of the ground state stimulation as it lies one molecular vibronic energy quantum (199 meV) below the main exciton transition $S_{0,v0} - S_{1,0} = 2.72\ eV(Exc1)$. The Raman spectrum in Fig.S2 reveals energies, relative intensities and characteristic decay rates of vibrons in the 100 nm neat polymer film. The polymer exhibits two main vibronic resonances, namely: V1 - 164 meV corresponding to inter-ring CC stretching oscillations (i.e. along the line of the chemical bond) and a doublet V2 of 194 and 199 meV attributed to aromatic intra-ring CC stretching modes.

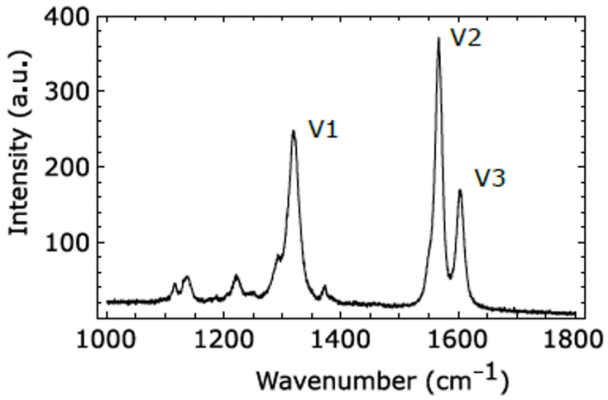

FIG. S2. Raman spectrum of the neat 100 nm spin-cast MeLPPP film on fused silica, measured at $\lambda_{ex} = 532\ nm$, where $V1, V2, V3$ correspond to the main vibronic peaks at 1320 cm^{-1}, 1568 cm^{-1} and 1604 cm^{-1} respectively.

Fig. S3a shows reflectivity map that reveals dispersion relation of the lower polariton branch at wide range of angles beyond the range accessed with angle-resolved photoluminescence (PL) measurements. The system demonstrates inflection in the lower polariton branch at high in-plane momenta, as well as evidence of normal mode splitting. In Fig. S3b we plot photoluminescence data acquired in the linear regime $0.6P_{th}$ (below polariton condensation) that shows polariton eigenstates at small wave-vectors within $\pm 16°$.

We employed a standard coupled harmonic oscillator model to fit experimental data. Fig. S3c represents the best-fit results of dispersion relations extracted from the experimental data, where black diamonds and open circles correspond to reflectivity data and red circles to the PL data from Fig. S3a and b respectively. We obtained vacuum Rabi splitting $2\hbar\Omega = 160\ meV$ for the interaction of $S_{0,0} \rightarrow S_{1,0}$ transition ($Exc1 = 2.72\ eV$) with the negatively detuned ($\Delta = -150\ meV$) cavity mode ($Cav = 2.57\ eV$). The splitting agrees

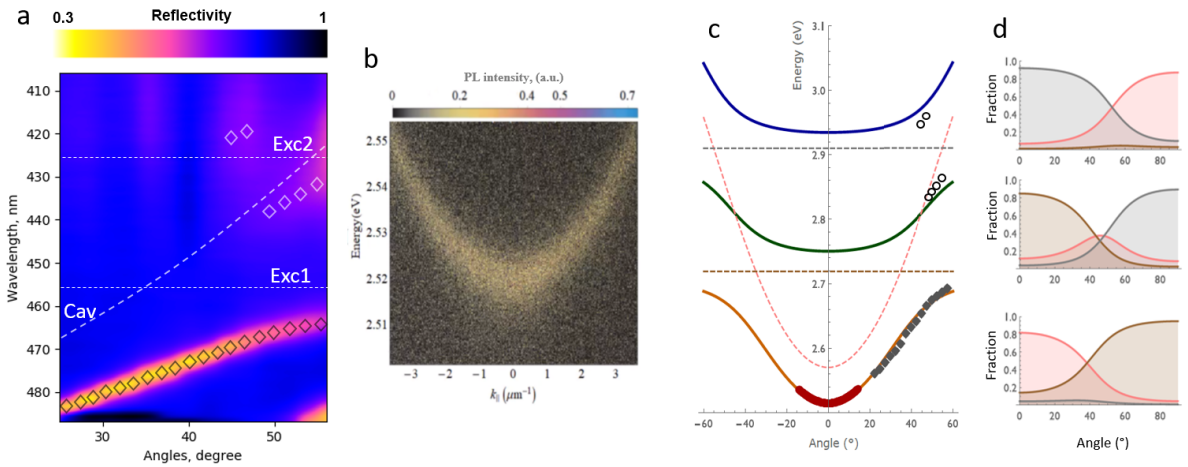

FIG. S3. Reflectivity map of the sample at the negative exciton cavity mode detuning (a), where black and white open diamond symbols show reflectivity minima of the lower and middle, upper polariton branches. Dashed white lines represent the bare cavity mode (Cav), $S_{0,0} \rightarrow S_{1,0}$ (Exc1) and $S_{0,0} \rightarrow S_{1,1}$ (Exc2) excitonic transitions. Angle-resolved PL spectra of the sample measured below condensation threshold at 0.6Pth (b). Polariton dispersion relations (c), where reflectivity peak positions from (a) (black diamond and black open circle symbols for the lower and middle, upper polariton branch respectively) are extended with photoluminescence peak positions of the lower polariton branch from (b) (red circle symbols). The polariton eigenenergies calculated from the coupled oscillator model are represented with orange, green and blue solid curves for the lower, middle and upper branches respectively. The uncoupled energies of the cavity mode, $S_{0,0} \rightarrow S_{1,0}$ and $S_{0,0} \rightarrow S_{1,1}$ transitions are displayed as red, brown and grey dashed lines. The composition of the polariton wavefunction (d) calculated from the Hopfield coefficients is shown for the upper (top), middle (center), and lower (bottom) polariton branches (photon - red, $S_{0,0} \rightarrow S_{1,0}$ - brown and $S_{0,0} \rightarrow S_{1,1}$ - grey).

well with the values obtained at lower detunings [1, 2]. Indeed the coupling strength $2\hbar\Omega$ does not depend on the detuning parameter but relies on an oscillator strength of $S_{0,0} \rightarrow S_{1,0}$ transition and cavity mode volume. In Fig. S3d we plot composition of the polariton wave functions in terms of exciton and photon fractions calculated from the Hopfield coefficients is shown for the upper (top), middle (center), and lower (bottom) polariton branches. The ground polariton state contains 82% of photonic and 14% and 4% of (0-0) and (0-1) excitonic fractions respectively.

II. SPONTANEOUSLY-FORMED AND SEEDED POLARITON CONDENSATES

Following experimental details described in Methods, we perform dispersion imaging for a range of pump fluence. Figure 1b of the main text shows the incident pump fluence dependencies of the emission intensity from the ground polariton state integrated over $\pm 0.2 \mu \mathrm{m}^{-1}$. In this section we provide in-depth analysis of spectral properties of the ground state emission for both: spontaneously-formed and seeded polariton condensates. At low pump fluence we observe a uniform distribution of polariton density along the states at the lower polariton branch, while for ∼twice higher pump fluence we observe a collapse of polariton distribution at the ground polariton state indicating polariton condensation. Figure S4a shows polariton distributions at $0.6P_{th}$ and $1.2P_{th}$, where $P_{th} = 42\mu J\ cm^{-2}$ is the threshold incident pump fluence of the spontaneously-formed polariton condensate. The process of polariton condensation is accompanied by the build-up of temporal coherence witnessed through the line narrowing and high-energy shift (so-called blueshift) due to nonlinearity of the matter component of polariton wave-function as shown in Figure S4b and c respectively.

The seed beam optically injects polaritons into the ground state leading to a substantial increase of polariton density. Such an increase is the result of several effects constructively contributing to the ground state population. First of all, optically injected polaritons accelerate energy relaxation from the exciton reservoir due to bosonic stimulation into the seeded states. It significantly improves the overall efficiency of exciton-to-polariton energy conversion. Being accelerated the exciton-to-polariton relaxation channel competes with ultra-fast intermolecular energy transfer - the detrimental effect preventing polariton condensation in disordered organic media [3]; and leads to ∼twice lower condensation threshold with respect to the unseeded process. Moreover, the seeded states are populated stronger than other states within the lower polariton branch facilitating lower condensation threshold as well. Figure S4d shows seeded polariton distribution along the lower branch below ($P = 0.5P'_{th}$ - left) and above ($P = 1.2P'_{th}$ - right) the threshold, where $P'_{th} = 27\mu J\ cm^{-2}$ is the threshold value expressed in terms of incident pump fluence. The energy of the seed beam is equal to 460 aJ defined as the incident pulse energy, i.e. before sample, that spectrally covers a full linewidth of the ground polariton state at $\pm 0.2\ \mu m^{-1}$. Importantly, unlike the abrupt line narrowing and blueshift nearby the threshold of unseeded condensation, the seeded process demonstrates a gradual transition from incoherent to the coherent state. Figures S4e and f

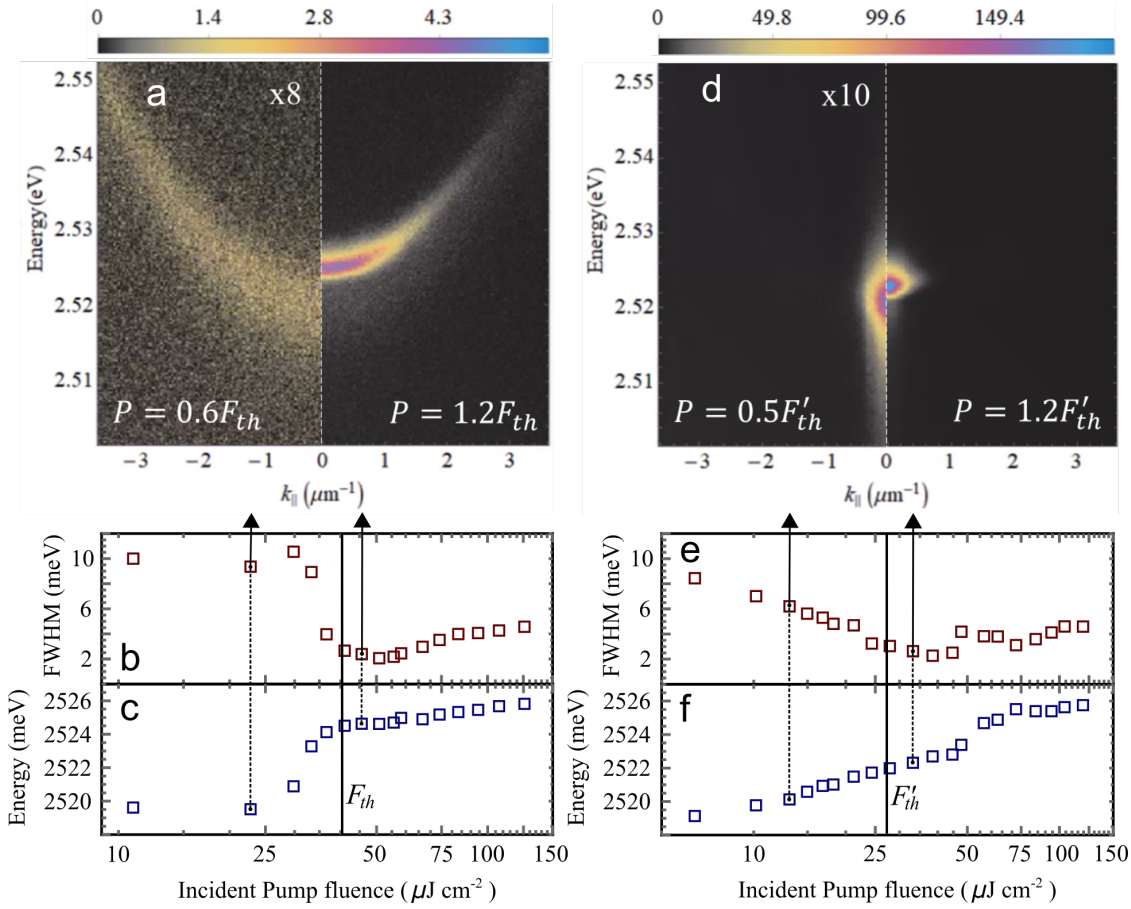

FIG. S4. **a**, *(E,k)* - distributions of polariton population along the lower polariton branch below (left) and above (right) the threshold of the spontaneously-formed condensate. **b** and **c**, Full width at half maximum and a peak energy of emission from the ground polariton state integrated over $\pm 0.2\mu\text{m}^{-1}$ in the spontaneous regime. **d**, *(E,k)* - distributions of polariton population along the lower polariton branch below (left) and above (right) the threshold of the seeded condensate. **e** and **f**, Full width at half maximum (FWHM) and a peak energy of emission from the ground polariton state integrated over $\pm 0.2\mu\text{m}^{-1}$ in the seeded regime. Solid vertical lines show condensation threshold in terms of incident pump fluence evaluated from Figure 1b in the main text. Arrows set correspondence of FWHM and Energy data with *(E,k)* - distributions.

show FWHM and a peak energy of emission from the ground polariton state integrated over $\pm 0.2\mu\text{m}^{-1}$ in the seeded regime. Such a smooth crossover to the condensate is the result of suppressed intermolecular energy transfer which is shown to be the origin of abrupt spectral changes at the condensation threshold [3]. With increasing pump fluence different nonlinear processes start playing a role. Their net contribution leads to the ongoing blueshift of the

ground polariton state and line broadening.

Finally, we would like to highlight the very high efficiency of vibron-mediated single-step polariton condensation in the polymer-based system. The given incident fluence of 42 $\mu J/cm^2$ at the threshold of the spontaneously-formed condensate leads to 8 $\mu J/cm^2$ in terms of the absorbed value taking into account the reflectance of the beam at 45 degree of incidence ($R = 0.81$) and slight elongation of the beam along the horizontal axis (Gaussian spot with 20 μm $\times$32 μm size at full width at half maximum). This estimation provides an upper boundary of the absorbed fluence in our experiments as we assume 19% of incident energy is absorbed by the structure. The value sets today the lowest threshold energy for polariton condensation in organic microcavities. Although the energy required to form a condensate without using any seed beam is at the level of the lowest value already, the seeded condensate takes even lower energy density with the threshold at $5\mu J\ cm^{-2}$. Our comparative analysis of absorbed pump fluence shows both regimes demonstrate outstanding low condensation thresholds among all existing organic material platforms, see Table S1.

TABLE S1. List of absorbed pump fluence at the condensation threshold reported up to date in various strongly-coupled organic microcavities. The value in brackets corresponds to the seeded polariton condensation

Cavity material	Absorbed pump fluence	Ref.
MeLPPP	8 (5) $\mu J/cm^2$	This work
Pentafluorene	12 $\mu J/cm^2$	[5]
2L-F, Ladder-type Oligo(p-phenylene)	12 $\mu J/cm^2$	[6]
PFO, Poly(9,9-dioctylfluorene)	19 $\mu J/cm^2$	[7]
TDAF, Ter(9,9-diarylfluorene)	30 $\mu J/cm^2$	[8]
BODIPY	120 $\mu J/cm^2$	[3]
Anthracene	320 $\mu J/cm^2$	[9]

III. MICROSCOPIC THEORY OF VIBRON-MEDIATED POLARITON CONDENSATION

We consider a nonequilibrium microscopic model which describes an ensemble of organic molecules with vibrationally dressed electronic transitions and coupled to cavity modes carrying different in-plane momenta $\hbar\mathbf{k}_{\parallel}$ (hereinafter $\hbar\mathbf{k}$). The electronic transition being localised at molecules are effectively treated as Frenkel-type excitons, where each excitation can be described by the Pauli creation and annihilation operators acting on a single molecule. Hereby, the full Hamiltonian of the systems reads:

$$\hat{H} = \hat{H}_{\text{cav}} + \hat{H}_{\text{exc}} + \hat{H}_{\text{vib}} + \hat{H}_{\text{exc-cav}} + \hat{H}_{\text{exc-vib}} \tag{1}$$

The Hamiltonian of the cavity $\hat{H}_{\text{cav}}$ is

$$\hat{H}_{\text{cav}} = \sum_{\mathbf{k}} \hbar\omega_{\text{cav}\mathbf{k}} \hat{a}^{\dagger}_{\text{cav}\mathbf{k}} \hat{a}_{\text{cav}\mathbf{k}} \tag{2}$$

where $\hat{a}^{\dagger}_{\text{cav}\mathbf{k}}$ and $\hat{a}_{\text{cav}\mathbf{k}}$ are the creation and annihilation operators for a photon in the cavity which obey commutation relation $\left[\hat{a}_{\text{cav}\mathbf{k}}, \hat{a}^{\dagger}_{\text{cav}\mathbf{k}'}\right] = \delta_{\mathbf{k},\mathbf{k}'}$, the wavevector $\mathbf{k}$ corresponds to in-plane momentum $\hbar\mathbf{k}$, and $\omega_{\text{cav}\mathbf{k}}$ is the eigenfrequency of the cavity mode with the in-plane wavevector $\mathbf{k}$.

The Hamiltonian of the excitons $\hat{H}_{\text{exc}}$ is

$$\hat{H}_{\text{exc}} = \sum_{j} \hbar\omega_{\text{exc}} \hat{\sigma}^{\dagger}_{\text{exc}j} \hat{\sigma}_{\text{exc}j} \tag{3}$$

where ω_{exc} is the eigenfrequency of the excitons, $\hat{\sigma}^{\dagger}_{\text{exc}j}$ and $\hat{\sigma}_{\text{exc}j}$ are the creation and annihilation operators of the exciton of a single conjugated segment of MeLPPP located at the point $\mathbf{r}_j$. These operators obey the anti-commutation relation $\hat{\sigma}_{\text{exc}j}\hat{\sigma}^{\dagger}_{\text{exc}j'} + \hat{\sigma}^{\dagger}_{\text{exc}j'}\hat{\sigma}_{\text{exc}j} = \delta_{j,j'}$. Below we consider the case of small probability for the exciton to be found in an excited state. In this case the approximate commutation relation $\left[\hat{\sigma}_{\text{exc}j}, \hat{\sigma}^{\dagger}_{\text{exc}j'}\right] \approx \delta_{j,j'}$ is valid.

The Hamiltonian of interaction between excitons and cavity modes $\hat{H}_{\text{exc-cav}}$ is a multi-mode Jaynes-Cummings Hamiltonian [13]

$$\hat{H}_{\text{exc-cav}} = \sum_{\mathbf{k},j} \hbar\Omega_{1\text{R}\mathbf{k}} \left(\hat{\sigma}^{\dagger}_{\text{exc}j} \hat{a}_{\text{cav}\mathbf{k}} e^{i\mathbf{k}\mathbf{r}_j} + \hat{\sigma}_{\text{exc}j} \hat{a}^{\dagger}_{\text{cav}\mathbf{k}} e^{-i\mathbf{k}\mathbf{r}_j} \right) \tag{4}$$

where $\Omega_{1\text{R}\mathbf{k}}$ is the Rabi frequency of interaction between an exciton placed at $\mathbf{r}_j$ and a cavity mode with the in-plane wavevector $\mathbf{k}$. Here we suppose that the electric field of the $\mathbf{k}$th

mode is distributed in the plane parallel to the mirrors according to $e^{i\mathbf{kr}}$ and constant in the anti-node position where the MeLPPP layer is located. This is a reasonable approximation since we deal with the microcavity carrying a single fundamental $\lambda/2$ mode and containing 35 nm thin MeLPPP layer at the center, which is much smaller than the wavelength λ. The explicit expression for the Rabi frequency is $\Omega_{1\mathrm{R}\mathbf{k}} = -\mathbf{E}_{\mathbf{k}}\mathbf{d}/\hbar$, where $\mathbf{d}$ is the transition dipole momentum of the exciton and $E_{\mathbf{k}}$ is the electric field amplitude per "one photon" in the cavity with the in-plane momentum $\hbar\mathbf{k}$.

It is convenient to introduce the collective operator effectively describing all excitons, namely,

$$\hat{c}_{\mathrm{exc}\mathbf{k}} = \frac{1}{\sqrt{N_{\mathrm{mol}}}} \sum_j \hat{\sigma}_{\mathrm{exc}j} e^{i\mathbf{k}\mathbf{r}_j} \tag{5}$$

where N_{mol} is the total number of MeLPPP π–conjugated segments and $\mathbf{k}$ is the wavevector. Operators $\hat{c}^{\dagger}_{\mathrm{exc}\mathbf{k}}$ and $\hat{c}_{\mathrm{exc}\mathbf{k}}$ are the creation and annihilation operators of the excitons which obey commutation relation $\left[\hat{c}_{\mathrm{exc}\mathbf{k}}, \hat{c}^{\dagger}_{\mathrm{exc}\mathbf{k}'}\right] = \delta_{\mathbf{k},\mathbf{k}'}$. Using the operators $\hat{c}_{\mathrm{exc}\mathbf{k}}$ we rewrite the Hamiltonians (3) and (4) in the following form

$$\hat{H}_{\mathrm{exc}} = \sum_{\mathbf{k}} \hbar\omega_{\mathrm{exc}} \hat{c}^{\dagger}_{\mathrm{exc}\mathbf{k}} \hat{c}_{\mathrm{exc}\mathbf{k}} \tag{6}$$

where $\omega_{\mathrm{exc}\mathbf{k}}$ is the eigenfrequency of the exciton with the wavevector $\mathbf{k}$ and Hamiltonian (4) in the following form

$$\hat{H}_{\mathrm{exc-cav}} = \sum_{\mathbf{k}} \hbar\Omega_{\mathrm{R}\mathbf{k}} \left(\hat{c}^{\dagger}_{\mathrm{exc}\mathbf{k}} \hat{a}_{\mathrm{cav}\mathbf{k}} + \hat{c}_{\mathrm{exc}\mathbf{k}} \hat{a}^{\dagger}_{\mathrm{cav}\mathbf{k}} \right) \tag{7}$$

where $\Omega_{\mathrm{R}\mathbf{k}} = \sqrt{N_{\mathrm{mol}}}\Omega_{1\mathrm{R}\mathbf{k}}$ is the Rabi frequency of exciton-photon interaction for the excitons and the cavity mode with $\hbar\mathbf{k}$ in-plane momentum.

The Hamiltonian of vibrons $\hat{H}_{\mathrm{vib}}$ is

$$\hat{H}_{\mathrm{vib}} = \sum_j \hbar\omega_{\mathrm{vib}} \hat{b}^{\dagger}_j \hat{b}_j \tag{8}$$

where $\hat{b}^{\dagger}_j$ and $\hat{b}_j$ are the creation and annihilation operators of vibrons which obey commutation relation $\left[\hat{b}_j, \hat{b}^{\dagger}_{j'}\right] = \delta_{j,j'}$.

The Hamiltonian of the interaction between the excitons and vibrons at a conjugated segment of MeLPPP is a standard optomechanical Hamiltonian [11]

$$\hat{H}_{\mathrm{exc-vib}} = \sum_j \hbar g \hat{\sigma}^{\dagger}_j \hat{\sigma}_j \left(\hat{b}_j + b^{\dagger}_j \right) \tag{9}$$

where the g is the interaction constant between the excitons and vibrons.

Following the same momentum space representation, it is convenient to introduce collective vibron operators according to

$$\hat{b}_{\mathbf{q}} = \frac{1}{\sqrt{N_{\mathrm{mol}}}} \sum_j \hat{b}_j e^{i\mathbf{q}\mathbf{r}_j} \tag{10}$$

Under the transformation (5) and (10) the Hamiltonian of collective vibrons $\hat{b}_{\mathbf{k}}$ and its interaction with collective excitons $\hat{c}_{\mathrm{exc}\mathbf{k}}$ takes the form

$$\hat{H}_{\mathrm{vib}} = \sum_{\mathbf{q}} \hbar\omega_{\mathrm{vib}} \hat{b}^{\dagger}_{\mathbf{q}} \hat{b}_{\mathbf{q}} \tag{11}$$

$$\hat{H}_{\mathrm{exc-vib}} = \sum_{\mathbf{k}} \sum_{\mathbf{k}'} \hbar g \hat{c}^{\dagger}_{\mathrm{exc}\mathbf{k}} \hat{c}_{\mathrm{exc}\mathbf{k}'} \left(\hat{b}^{\dagger}_{-(\mathbf{k}-\mathbf{k}')} + \hat{b}_{\mathbf{k}-\mathbf{k}'} \right) \tag{12}$$

where $\hat{b}^{\dagger}_{\mathbf{q}}$ and $\hat{b}_{\mathbf{q}}$ are the creation and annihilation operators of the vibrons which obey commutation relation $\left[\hat{b}_{\mathbf{q}}, \hat{b}^{\dagger}_{\mathbf{q}'}\right] = \delta_{\mathbf{q},\mathbf{q}'}$, the vector $\mathbf{q}$ is in-plane wavevector of the vibrons, ω_{vib} is the eigenfrequency of the vibrons with the in-plane wavevector $\mathbf{q}$. Note that momenta of excitons and vibrons in Eq. (12) fulfil momentum conservation law.

Next, we diagonalize the light-matter interaction part of the Hamiltonian [13], namely $\hat{H}_{\mathrm{cav}} + \hat{H}_{\mathrm{exc}} + \hat{H}_{\mathrm{exc-cav}}$. In the new basis of exciton–polariton states, annihilation operators for the lower $\hat{s}_{\mathrm{low}\mathbf{k}}$ and upper $\hat{s}_{\mathrm{up}\mathbf{k}}$ polaritons can be expressed through the standard transformation relations:

$$\hat{s}_{\mathrm{low}\mathbf{k}} = \hat{a}_{\mathrm{cav}\mathbf{k}} \cos\varphi_{\mathbf{k}} - \hat{c}_{\mathrm{exc}\mathbf{k}} \sin\varphi_{\mathbf{k}} \tag{13}$$

$$\hat{s}_{\mathrm{up}\mathbf{k}} = \hat{c}_{\mathrm{exc}\mathbf{k}} \cos\varphi_{\mathbf{k}} + \hat{a}_{\mathrm{cav}\mathbf{k}} \sin\varphi_{\mathbf{k}} \tag{14}$$

where

$$\varphi_{\mathbf{k}} = \frac{1}{2} \mathrm{arctg} \left(\frac{2\Omega_{\mathrm{R}\mathbf{k}}}{\omega_{\mathrm{exc}} - \omega_{\mathrm{cav}\mathbf{k}}} \right) \tag{15}$$

Following the transformations above the full Hamiltonian (1) takes the form:

$$\begin{aligned} \hat{H} = &\sum_{\mathbf{k}} \hbar\omega_{\mathrm{up}\mathbf{k}} \hat{s}^{\dagger}_{\mathrm{up}\mathbf{k}} \hat{s}_{\mathrm{up}\mathbf{k}} + \sum_{\mathbf{k}} \hbar\omega_{\mathrm{low}\mathbf{k}} \hat{s}^{\dagger}_{\mathrm{low}\mathbf{k}} \hat{s}_{\mathrm{low}\mathbf{k}} + \sum_{\mathbf{q}} \hbar\omega_{\mathrm{vib}} \hat{b}^{\dagger}_{\mathbf{q}} \hat{b}_{\mathbf{q}} + \\ &+ \sum_{\mathbf{k}} \sum_{\mathbf{k}'} \hbar g \left(\hat{s}^{\dagger}_{\mathrm{up}\mathbf{k}} \cos\varphi_{\mathbf{k}} - \hat{s}^{\dagger}_{\mathrm{low}\mathbf{k}} \sin\varphi_{\mathbf{k}} \right) \left(\hat{s}_{\mathrm{up}\mathbf{k}'} \cos\varphi_{\mathbf{k}'} - \hat{s}_{\mathrm{low}\mathbf{k}'} \sin\varphi_{\mathbf{k}'} \right) \left(\hat{b}^{\dagger}_{-(\mathbf{k}-\mathbf{k}')} + \hat{b}_{\mathbf{k}-\mathbf{k}'} \right) \end{aligned} \tag{16}$$

where the new eigenfrequencies are:

$$\omega_{\mathrm{low}\mathbf{k}} = (\omega_{\mathrm{exc}} + \omega_{\mathrm{cav}\mathbf{k}})/2 - \sqrt{(\omega_{\mathrm{exc}} - \omega_{\mathrm{cav}\mathbf{k}})^2/4 + \Omega_{\mathrm{R}\mathbf{k}}^2} \tag{17}$$

$$\omega_{\mathrm{up}\mathbf{k}} = (\omega_{\mathrm{exc}} + \omega_{\mathrm{cav}\mathbf{k}})/2 + \sqrt{(\omega_{\mathrm{exc}} - \omega_{\mathrm{cav}\mathbf{k}})^2/4 + \Omega_{\mathrm{R}\mathbf{k}}^2} \tag{18}$$

In turn, lower and upper polaritons as well as vibrons interact with the environment that inevitably leads to the relaxation processes. We consider the relaxation processes by means of Lindblad superoperators [12, 13] acting on the general density matrix $\hat{\rho}$ which ultimately describes the entire system including all the polaritons and vibrons. The Lindblad superoperators for the lower, upper polaritons and vibrons are

$$\hat{L}_{\mathrm{low}}(\hat{\rho}) = \sum_{\mathbf{k}} \frac{\gamma_{\mathrm{low}\mathbf{k}}}{2} \left(2\hat{s}_{\mathrm{low}\mathbf{k}} \hat{\rho} \hat{s}^{\dagger}_{\mathrm{low}\mathbf{k}} - \hat{s}^{\dagger}_{\mathrm{low}\mathbf{k}} \hat{s}_{\mathrm{low}\mathbf{k}} \hat{\rho} - \hat{\rho} \hat{s}^{\dagger}_{\mathrm{low}\mathbf{k}} \hat{s}_{\mathrm{low}\mathbf{k}} \right) \tag{19}$$

$$\hat{L}_{\mathrm{up}}(\hat{\rho}) = \sum_{\mathbf{k}} \frac{\gamma_{\mathrm{up}\mathbf{k}}}{2} \left(2\hat{s}_{\mathrm{up}\mathbf{k}} \hat{\rho} \hat{s}^{\dagger}_{\mathrm{up}\mathbf{k}} - \hat{s}^{\dagger}_{\mathrm{up}\mathbf{k}} \hat{s}_{\mathrm{up}\mathbf{k}} \hat{\rho} - \hat{\rho} \hat{s}^{\dagger}_{\mathrm{up}\mathbf{k}} \hat{s}_{\mathrm{up}\mathbf{k}} \right) \tag{20}$$

$$\hat{L}_{\mathrm{vib}}(\hat{\rho}) = \sum_{\mathbf{q}} \frac{\gamma_{\mathrm{vib}}}{2} \left(1 + n^{\mathrm{th}}_{\mathrm{vib}}\right) \left(2\hat{b}_{\mathbf{q}} \hat{\rho} \hat{b}^{\dagger}_{\mathbf{q}} - \hat{b}^{\dagger}_{\mathbf{q}} \hat{b}_{\mathbf{q}} \hat{\rho} - \hat{\rho} \hat{b}^{\dagger}_{\mathbf{q}} \hat{b}_{\mathbf{q}} \right) + \sum_{\mathbf{q}} \frac{\gamma_{\mathrm{vib}}}{2} n^{\mathrm{th}}_{\mathrm{vib}} \left(2\hat{b}^{\dagger}_{\mathbf{q}} \hat{\rho} \hat{b}_{\mathbf{q}} - \hat{b}_{\mathbf{q}} \hat{b}^{\dagger}_{\mathbf{q}} \hat{\rho} - \hat{\rho} \hat{b}_{\mathbf{q}} \hat{b}^{\dagger}_{\mathbf{q}} \right) \tag{21}$$

where $\gamma_{\mathrm{low}\mathbf{k}}$, $\gamma_{\mathrm{up}\mathbf{k}}$ and γ_{vib} are the dissipation rates of lower, upper polaritons and the vibrons respectively, and $n^{\mathrm{th}}_{\mathrm{vib}} = 1/(\exp(\hbar\omega_{\mathrm{vib}}/k_B T) - 1)$ is the thermal distribution of vibrons at an environment temperature T and k_B is the Boltzmann constant.

Thermalization of the lower polaritons is described by the following Lindblad superoperator:

$$\hat{L}_{\mathrm{th}}(\hat{\rho}) = \sum_{\mathbf{k}_1, \mathbf{k}_2} \frac{\gamma^{\mathbf{k}_1 \mathbf{k}_2}_{\mathrm{low}}}{2} \left(2\hat{s}_{\mathrm{low}\mathbf{k}_2} \hat{s}^{\dagger}_{\mathrm{low}\mathbf{k}_1} \hat{\rho} \hat{s}_{\mathrm{low}\mathbf{k}_1} \hat{s}^{\dagger}_{\mathrm{low}\mathbf{k}_2} - \hat{s}_{\mathrm{low}\mathbf{k}_1} \hat{s}^{\dagger}_{\mathrm{low}\mathbf{k}_2} \hat{s}_{\mathrm{low}\mathbf{k}_2} \hat{s}^{\dagger}_{\mathrm{low}\mathbf{k}_1} \hat{\rho} - \hat{\rho} \hat{s}_{\mathrm{low}\mathbf{k}_1} \hat{s}^{\dagger}_{\mathrm{low}\mathbf{k}_2} \hat{s}_{\mathrm{low}\mathbf{k}_2} \hat{s}^{\dagger}_{\mathrm{low}\mathbf{k}_1} \right) \tag{22}$$

here $\gamma^{\mathbf{k}_1 \mathbf{k}_2}_{\mathrm{low}}$ is the rate of energy flow from the lower polaritons having in-plane wavevector $\mathbf{k}_2$ towards ones with wavevector $\mathbf{k}_1$. According to the Kubo-Martin-Schwinger relation, the rate $\gamma^{\mathbf{k}_1 \mathbf{k}_2}_{\mathrm{low}}$ is defined as

$$\gamma^{\mathbf{k}_1 \mathbf{k}_2}_{\mathrm{low}} = \gamma^{\mathbf{k}_2 \mathbf{k}_1}_{\mathrm{low}} \exp\left(\frac{\hbar\omega_{\mathrm{low}\mathbf{k}_2} - \hbar\omega_{\mathrm{low}\mathbf{k}_1}}{k_B T} \right) \tag{23}$$

where T is the effective MeLPPP temperature.

The incoherent pump of the lower and upper polaritons is described by the Lindblad superoperator:

$$\hat{L}_{\text{pump}}(\hat{\rho}) = \sum_{\mathbf{k}} \frac{\kappa_{\text{low}\mathbf{k}}(t)}{2}\left(2\hat{s}_{\text{low}\mathbf{k}}\hat{\rho}\hat{s}^{\dagger}_{\text{low}\mathbf{k}} - \hat{s}^{\dagger}_{\text{low}\mathbf{k}}\hat{s}_{\text{low}\mathbf{k}}\hat{\rho} - \hat{\rho}\hat{s}^{\dagger}_{\text{low}\mathbf{k}}\hat{s}_{\text{low}\mathbf{k}}\right) + \sum_{\mathbf{k}} \frac{\kappa_{\text{low}\mathbf{k}}(t)}{2}\left(2\hat{s}^{\dagger}_{\text{low}\mathbf{k}}\hat{\rho}\hat{s}_{\text{low}\mathbf{k}} - \hat{s}_{\text{low}\mathbf{k}}\hat{s}^{\dagger}_{\text{low}\mathbf{k}}\hat{\rho} - \hat{\rho}\hat{s}_{\text{low}\mathbf{k}}\hat{s}^{\dagger}_{\text{low}\mathbf{k}}\right) + \sum_{\mathbf{k}} \frac{\kappa_{\text{up}\mathbf{k}}(t)}{2}\left(2\hat{s}_{\text{up}\mathbf{k}}\hat{\rho}\hat{s}^{\dagger}_{\text{up}\mathbf{k}} - \hat{s}^{\dagger}_{\text{up}\mathbf{k}}\hat{s}_{\text{up}\mathbf{k}}\hat{\rho} - \hat{\rho}\hat{s}^{\dagger}_{\text{up}\mathbf{k}}\hat{s}_{\text{up}\mathbf{k}}\right) + \sum_{\mathbf{k}} \frac{\kappa_{\text{up}\mathbf{k}}(t)}{2}\left(2\hat{s}^{\dagger}_{\text{up}\mathbf{k}}\hat{\rho}\hat{s}_{\text{up}\mathbf{k}} - \hat{s}_{\text{up}\mathbf{k}}\hat{s}^{\dagger}_{\text{up}\mathbf{k}}\hat{\rho} - \hat{\rho}\hat{s}_{\text{up}\mathbf{k}}\hat{s}^{\dagger}_{\text{up}\mathbf{k}}\right) \quad (24)$$

The seed to the lower polaritons is described by the Lindblad superoperator:

$$\hat{L}_{\text{seed}}(\hat{\rho}) = \sum_{\mathbf{k}} \frac{\kappa_{\text{seed}\mathbf{k}}(t)}{2}\left(2\hat{s}_{\text{low}\mathbf{k}}\hat{\rho}\hat{s}^{\dagger}_{\text{low}\mathbf{k}} - \hat{s}^{\dagger}_{\text{low}\mathbf{k}}\hat{s}_{\text{low}\mathbf{k}}\hat{\rho} - \hat{\rho}\hat{s}^{\dagger}_{\text{low}\mathbf{k}}\hat{s}_{\text{low}\mathbf{k}}\right) + \sum_{\mathbf{k}} \frac{\kappa_{\text{seed}\mathbf{k}}(t)}{2}\left(2\hat{s}^{\dagger}_{\text{low}\mathbf{k}}\hat{\rho}\hat{s}_{\text{low}\mathbf{k}} - \hat{s}_{\text{low}\mathbf{k}}\hat{s}^{\dagger}_{\text{low}\mathbf{k}}\hat{\rho} - \hat{\rho}\hat{s}_{\text{low}\mathbf{k}}\hat{s}^{\dagger}_{\text{low}\mathbf{k}}\right) \quad (25)$$

The resulting master equation is

$$\frac{d\hat{\rho}}{dt} = \frac{i}{\hbar}\left[\hat{\rho}, \hat{H}\right] + \hat{L}_{\text{up}}(\hat{\rho}) + \hat{L}_{\text{low}}(\hat{\rho}) + \hat{L}_{\text{vib}}(\hat{\rho}) + \hat{L}_{\text{th}}(\hat{\rho}) + \hat{L}_{\text{pump}}(\hat{\rho}) + \hat{L}_{\text{seed}}(\hat{\rho}) \quad (26)$$

Further on we develop a mean-field theory [12] for the system described above. We use the following definition $\left\langle \dot{\hat{A}} \right\rangle = \text{Tr}\left(\dot{\hat{\rho}}\hat{A}\right)$ and the master equation (26) to derive equations for the avarage polariton numbers $n_{\text{up}\mathbf{k}} = \left\langle \hat{s}^{\dagger}_{\text{up}\mathbf{k}}\hat{s}_{\text{up}\mathbf{k}} \right\rangle$, $n_{\text{low}\mathbf{k}} = \left\langle \hat{s}^{\dagger}_{\text{low}\mathbf{k}}\hat{s}_{\text{low}\mathbf{k}} \right\rangle$ and the energy flows between excitons and vibrons $J_{\text{up}\mathbf{k}\mathbf{k}'} = \left\langle \hat{s}_{\text{up}\mathbf{k}}\hat{s}^{\dagger}_{\text{low}\mathbf{k}'}\hat{b}^{\dagger}_{\mathbf{k}-\mathbf{k}'} \right\rangle$, $J_{\text{low}\mathbf{k}''\mathbf{k}'} = \left\langle \hat{s}_{\text{low}\mathbf{k}''}\hat{s}^{\dagger}_{\text{low}\mathbf{k}'}\hat{b}^{\dagger}_{\mathbf{k}''-\mathbf{k}'} \right\rangle$. Assuming that at any given time the number of excited vibrons are neglectible $n_{\text{vib}\mathbf{q}} = \left\langle \hat{b}^{\dagger}_{\mathbf{q}}\hat{b}_{\mathbf{q}} \right\rangle \ll 1$ we obtain

$$\frac{dn_{\text{up}\mathbf{k}}}{dt} = -\gamma_{\text{up}\mathbf{k}}\left(n_{\text{up}\mathbf{k}} - \frac{\kappa_{\text{up}\mathbf{k}}(t)}{\gamma_{\text{up}\mathbf{k}}}\right) + i\sum_{\mathbf{k}'} g\cos\varphi_{\mathbf{k}}\sin\varphi_{\mathbf{k}'}\left(J^{*}_{\text{up}\mathbf{k}\mathbf{k}'} - J_{\text{up}\mathbf{k}\mathbf{k}'}\right) \quad (27)$$

$$\frac{dn_{\text{low}\mathbf{k}'}}{dt} = -\gamma_{\text{low}\mathbf{k}'}\left(n_{\text{low}\mathbf{k}'} - \frac{\kappa_{\text{low}\mathbf{k}'}(t)}{\gamma_{\text{low}\mathbf{k}'}} - \frac{\kappa_{\text{seed}\mathbf{k}'}(t)}{\gamma_{\text{low}\mathbf{k}'}}\right) - i\sum_{\mathbf{k}} g\cos\varphi_{\mathbf{k}}\sin\varphi_{\mathbf{k}'}\left(J^{*}_{\text{up}\mathbf{k}\mathbf{k}'} - J_{\text{up}\mathbf{k}\mathbf{k}'}\right) - i\sum_{\mathbf{k}''} g\sin\varphi_{\mathbf{k}''}sin\varphi_{\mathbf{k}'}\left(J^{*}_{\text{low}\mathbf{k}''\mathbf{k}'} - J_{\text{low}\mathbf{k}''\mathbf{k}'}\right) + i\sum_{\mathbf{k}''} g\sin\varphi_{\mathbf{k}''}\sin\varphi_{\mathbf{k}'}\left(J^{*}_{\text{low}\mathbf{k}'\mathbf{k}''} - J_{\text{low}\mathbf{k}'\mathbf{k}''}\right) + \sum_{\mathbf{k}''}\left\{\gamma^{\mathbf{k}'\mathbf{k}''}_{\text{low}}\left(n_{\text{low}\mathbf{k}'}+1\right)n_{\text{low}\mathbf{k}''} - \gamma^{\mathbf{k}''\mathbf{k}'}_{\text{low}}\left(n_{\text{low}\mathbf{k}''}+1\right)n_{\text{low}\mathbf{k}'}\right\} \quad (28)$$

$$\frac{dJ_{\mathrm{up}\mathbf{k}\mathbf{k}'}}{dt} = -i\left(\omega_{\mathrm{up}\mathbf{k}} - \omega_{\mathrm{low}\mathbf{k}'} - \omega_{\mathrm{vib}}\right) J_{\mathrm{up}\mathbf{k}\mathbf{k}'} - \frac{1}{2}\left(\gamma_{\mathrm{up}\mathbf{k}} + \gamma_{\mathrm{low}\mathbf{k}'} + \gamma_{\mathrm{vib}}\right) J_{\mathrm{up}\mathbf{k}\mathbf{k}'} - \\ - ig\cos\varphi_{\mathbf{k}}\sin\varphi_{\mathbf{k}'} n_{\mathrm{up}\mathbf{k}}\left(n_{\mathrm{low}\mathbf{k}'} + 1\right) \quad (29)$$

$$\frac{dJ_{\mathrm{low}\mathbf{k}''\mathbf{k}'}}{dt} = -i\left(\omega_{\mathrm{low}\mathbf{k}''} - \omega_{\mathrm{low}\mathbf{k}'} - \omega_{\mathrm{vib}}\right) J_{\mathrm{low}\mathbf{k}''\mathbf{k}'} - \frac{1}{2}\left(\gamma_{\mathrm{low}\mathbf{k}''} + \gamma_{\mathrm{low}\mathbf{k}'} + \gamma_{\mathrm{vib}}\right) J_{\mathrm{low}\mathbf{k}''\mathbf{k}'} - \\ - ig\sin\varphi_{\mathbf{k}''}\sin\varphi_{\mathbf{k}'} n_{\mathrm{low}\mathbf{k}''}\left(n_{\mathrm{low}\mathbf{k}'} + 1\right) \quad (30)$$

We exclude adiabatically energy flows $J_{\mathrm{up}\mathbf{k}\mathbf{k}'}$, $J_{\mathrm{low}\mathbf{k}''\mathbf{k}'}$ and arrive at

$$\frac{dn_{\mathrm{up}\mathbf{k}}}{dt} = -\gamma_{\mathrm{up}\mathbf{k}}\left(n_{\mathrm{up}\mathbf{k}} - \frac{\kappa_{\mathrm{up}\mathbf{k}}(t)}{\gamma_{\mathrm{up}\mathbf{k}}}\right) - \sum_{\mathbf{k}'} G_{\mathrm{up}\mathbf{k}\mathbf{k}'} n_{\mathrm{up}\mathbf{k}}\left(n_{\mathrm{low}\mathbf{k}'} + 1\right) \quad (31)$$

$$\frac{dn_{\mathrm{low}\mathbf{k}'}}{dt} = -\gamma_{\mathrm{low}\mathbf{k}'}\left(n_{\mathrm{low}\mathbf{k}'} - \frac{\kappa_{\mathrm{low}\mathbf{k}'}(t)}{\gamma_{\mathrm{low}\mathbf{k}'}} - \frac{\kappa_{\mathrm{seed}\mathbf{k}'}(t)}{\gamma_{\mathrm{low}\mathbf{k}'}}\right) + \sum_{\mathbf{k}'} G_{\mathrm{up}\mathbf{k}\mathbf{k}'} n_{\mathrm{up}\mathbf{k}}\left(n_{\mathrm{low}\mathbf{k}'} + 1\right) + \\ + \sum_{\mathbf{k}''} G_{\mathrm{low}\mathbf{k}''\mathbf{k}'} n_{\mathrm{low}\mathbf{k}''}\left(n_{\mathrm{low}\mathbf{k}'} + 1\right) - \sum_{\mathbf{k}''} G_{\mathrm{low}\mathbf{k}'\mathbf{k}''} n_{\mathrm{low}\mathbf{k}'}\left(n_{\mathrm{low}\mathbf{k}''} + 1\right) \\ + \sum_{\mathbf{k}''}\left\{\gamma_{\mathrm{low}}^{\mathbf{k}'\mathbf{k}''}\left(n_{\mathrm{low}\mathbf{k}'} + 1\right) n_{\mathrm{low}\mathbf{k}''} - \gamma_{\mathrm{low}}^{\mathbf{k}''\mathbf{k}'}\left(n_{\mathrm{low}\mathbf{k}''} + 1\right) n_{\mathrm{low}\mathbf{k}'}\right\} \quad (32)$$

where we denote

$$G_{\mathrm{up}\mathbf{k}\mathbf{k}'} = \frac{\left(g\cos\varphi_{\mathbf{k}}\sin\varphi_{\mathbf{k}'}\right)^2\left(\gamma_{\mathrm{up}\mathbf{k}} + \gamma_{\mathrm{low}\mathbf{k}'} + \gamma_{\mathrm{vib}}\right)}{\left(\omega_{\mathrm{up}\mathbf{k}} - \omega_{\mathrm{low}\mathbf{k}'} - \omega_{\mathrm{vib}}\right)^2 + \frac{1}{4}\left(\gamma_{\mathrm{up}\mathbf{k}} + \gamma_{\mathrm{low}\mathbf{k}'} + \gamma_{\mathrm{vib}}\right)^2} \quad (33)$$

$$G_{\mathrm{low}\mathbf{k}'\mathbf{k}''} = \frac{\left(g\sin\varphi_{\mathbf{k}'}\sin\varphi_{\mathbf{k}''}\right)^2\left(\gamma_{\mathrm{low}\mathbf{k}'} + \gamma_{\mathrm{low}\mathbf{k}''} + \gamma_{\mathrm{vib}}\right)}{\left(\omega_{\mathrm{low}\mathbf{k}'} - \omega_{\mathrm{low}\mathbf{k}''} - \omega_{\mathrm{vib}}\right)^2 + \frac{1}{4}\left(\gamma_{\mathrm{low}\mathbf{k}'} + \gamma_{\mathrm{low}\mathbf{k}''} + \gamma_{\mathrm{vib}}\right)^2} \quad (34)$$

We assume that

$$\kappa_{\mathrm{up}\mathbf{k}}(t) = \kappa_{\mathrm{pump}}(t)\,\delta\left(\mathbf{k} - \mathbf{k}_{\mathrm{pump}}\right), \quad \kappa_{\mathrm{low}\mathbf{k}'}(t) = \kappa_{\mathrm{pump}}(t)\,\delta\left(\mathbf{k}' - \mathbf{k}_{\mathrm{pump}}\right), \quad (35)$$

$$\kappa_{\mathrm{seed}\mathbf{k}}(t) = \kappa_{\mathrm{seed}}(t)\, e^{-|\mathbf{k}|^2/|K_{\mathrm{seed}}|^2}, \quad (36)$$

where K_{seed} is equal to 0.2 $\mu\mathrm{m}^{-1}$.

Further, we move from the set of wave vectors to a set of frequencies. Note that since Eqs. (31)-(32) contain the spontaneous term, $n_{\mathrm{low}\mathbf{k}'} + 1$, one should take into account the density of states. To numerically simulate the system dynamics, we consider a discrete finite set of frequencies (ω_0, ω_1, ω_2, ..., ω_N) with a sampling step equals to $\delta\omega$, that is $\omega_{j+1} - \omega_j = \delta\omega$, where N means the total number of sampled frequencies (in numerical

simulations, we choose $N = 120$). For the sake of simplicity we introduce the ground state frequency as $\omega_0 = \omega_{\mathrm{low}(\mathbf{k}=0)}$. To calculate the number of states within the frequency range $\omega_j - \delta\omega < \omega < \omega_j$ with $j = 1, ..., N$ we approximate the lower polariton dispersion with a quadratic dependence $\omega_{\mathrm{low}\mathbf{k}} = \omega_{\mathrm{low}(\mathbf{k}=0)} + \alpha_{\mathrm{cav}}\mathbf{k}^2$ so that it appears explicitly in the following form:

$$D_{\omega_j} = \sum_{\mathbf{k},\ \omega_j - \delta\omega < \omega_{\mathrm{low}\mathbf{k}} < \omega_j} 1 \approx \left(Ln_{\mathrm{MeLPPP}}^{1/3}\right) \frac{S}{(2\pi)^2} \int\limits_{\omega_j - \delta\omega < \omega_{\mathrm{low}\mathbf{k}} < \omega_j} d^2\mathbf{k} = \frac{S}{(2\pi)^2} \left(Ln_{\mathrm{MeLPPP}}^{1/3}\right) \frac{\pi}{\alpha}\delta\omega \tag{37}$$

where S is the area illuminated by the pump, L is the thickness of MeLPPP layer, n_{MeLPPP} is the density of chromophores in the MeLPPP layer. Unity in Eq. (37) denotes the one state with fixed wavevector $\mathbf{k}$. Note that the expression for D_{ω_j} is frequency independent in the case under consideration. If we substitute characteristic values of $S = 300\ \mu\mathrm{m}^2$, $L = 0.035\ \mu\mathrm{m}$, $n_{\mathrm{MeLPPP}} \approx 10^6\ \mu\mathrm{m}^{-3}$ and $\alpha_{\mathrm{cav}} = 2.2\ \mathrm{meV}\cdot\mu\mathrm{m}^2$, then we obtain $D_{\omega_j} \approx 10^5 \cdot \delta\omega$ where $\delta\omega$ is measured in eV.

We denote

$$n_{\mathrm{upP}} = n_{\mathrm{up}\mathbf{k}_{\mathrm{pump}}}, \quad \omega_{\mathrm{upP}} = \omega_{\mathrm{up}\mathbf{k}_{\mathrm{pump}}}, \quad \gamma_{\mathrm{upP}} = \gamma_{\mathrm{up}\mathbf{k}_{\mathrm{pump}}} \tag{38}$$

$$n_{\mathrm{lowP}} = n_{\mathrm{low}\mathbf{k}_{\mathrm{pump}}}, \quad \omega_{\mathrm{lowP}} = \omega_{\mathrm{low}\mathbf{k}_{\mathrm{pump}}}, \quad \gamma_{\mathrm{lowP}} = \gamma_{\mathrm{low}\mathbf{k}_{\mathrm{pump}}} \tag{39}$$

$$n_{\mathrm{low}\omega_j} = \sum_{\mathbf{k}',\ \omega_j - \delta\omega < \omega_{\mathrm{low}\mathbf{k}'} < \omega_j} n_{\mathrm{low}\mathbf{k}'}, \quad \omega_{\mathrm{low}\omega_j} = \omega_j, \quad \gamma_{\mathrm{low}\omega_j} = \gamma_{\mathrm{low}\mathbf{k}'}\big|_{\omega_{\mathrm{low}\mathbf{k}'} = \omega_j} \tag{40}$$

$$\kappa_{\mathrm{seed}\omega_j}(t) = \sum_{\mathbf{k}',\ \omega_j - \delta\omega < \omega_{\mathrm{low}\mathbf{k}'} < \omega_j} \kappa_{\mathrm{seed}\mathbf{k}'}(t) \tag{41}$$

$$n_{\mathrm{low}0} = n_{\mathrm{low}\mathbf{k}'=0}, \quad \omega_{\mathrm{low}0} = \omega_{\mathrm{low}\mathbf{k}'=0}, \quad \gamma_{\mathrm{low}0} = \gamma_{\mathrm{low}\mathbf{k}'=0} \tag{42}$$

$$\gamma_{\mathrm{low}}^{\omega_j\omega_m} = \gamma_{\mathrm{low}}^{\mathbf{k}'\mathbf{k}''}\Big|_{\omega_{\mathrm{low}\mathbf{k}'} = \omega_j,\, \omega_{\mathrm{low}\mathbf{k}''} = \omega_m}, \quad \gamma_{\mathrm{low}}^{0\omega_j} = \gamma_{\mathrm{low}}^{\mathbf{k}'\mathbf{k}''}\Big|_{\mathbf{k}'=0,\, \omega_{\mathrm{low}\mathbf{k}''} = \omega_j}, \quad \gamma_{\mathrm{low}}^{\omega_j 0} = \gamma_{\mathrm{low}}^{\mathbf{k}'\mathbf{k}''}\Big|_{\omega_{\mathrm{low}\mathbf{k}'} = \omega_j,\, \mathbf{k}''=0} \tag{43}$$

$$\varphi_{\mathrm{P}} = \varphi_{\mathbf{k}_{\mathrm{pump}}}, \quad \varphi_{\omega_j} = \varphi_{\mathbf{k}}\big|_{\omega_{\mathrm{low}\mathbf{k}} = \omega_j}, \quad \varphi_0 = \varphi_{\mathbf{k}=0} \tag{44}$$

where $j = 1, ..., N$. As a result we obtain the discrete set of equations

$$\frac{dn_{\mathrm{upP}}}{dt} = -\gamma_{\mathrm{upP}}\left(n_{\mathrm{upP}} - \frac{\kappa_{\mathrm{pump}}(t)}{\gamma_{\mathrm{upP}}}\right) - \sum_{j=1}^{N} G_{\mathrm{up}\omega_j} n_{\mathrm{upP}}\left(n_{\mathrm{low}\omega_j} + D_{\omega_j}\right) - G_{\mathrm{up}0} n_{\mathrm{upP}}\left(n_{\mathrm{low}0} + 1\right) \tag{45}$$

$$\frac{dn_{\mathrm{lowP}}}{dt} = -\gamma_{\mathrm{lowP}}\left(n_{\mathrm{lowP}} - \frac{\kappa_{\mathrm{pump}}(t)}{\gamma_{\mathrm{lowP}}}\right) - \sum_{j=1}^{N} G_{\mathrm{low}\omega_j} n_{\mathrm{lowP}}\left(n_{\mathrm{low}\omega_j} + D_{\omega_j}\right) - G_{\mathrm{low}0} n_{\mathrm{lowP}}\left(n_{\mathrm{low}0} + 1\right) \tag{46}$$

$$\frac{dn_{\mathrm{low}\omega_j}}{dt} = -\gamma_{\mathrm{low}\omega_j}\left(n_{\mathrm{low}\omega_j} - \frac{\kappa_{\mathrm{seed}\omega_j}(t)}{\gamma_{\mathrm{low}\omega_j}}\right) + \\ + G_{\mathrm{up}\omega_j} n_{\mathrm{upP}}\left(n_{\mathrm{low}\omega_j} + D_{\omega_j}\right) + G_{\mathrm{low}\omega_j} n_{\mathrm{lowP}}\left(n_{\mathrm{low}\omega_j} + D_{\omega_j}\right) + \\ + \sum_{m=1}^{N}\left\{\gamma_{\mathrm{low}}^{\omega_j\omega_m}\left(n_{\mathrm{low}\omega_j} + D_{\omega_j}\right) n_{\mathrm{low}\omega_m} - \gamma_{\mathrm{low}}^{\omega_m\omega_j}\left(n_{\mathrm{low}\omega_m} + D_{\omega_m}\right) n_{\mathrm{low}\omega_j}\right\} + \\ + \left\{\gamma_{\mathrm{low}}^{\omega_j 0}\left(n_{\mathrm{low}\omega_j} + D_{\omega_j}\right) n_{\mathrm{low}0} - \gamma_{\mathrm{low}}^{0\omega_j}\left(n_{\mathrm{low}0} + 1\right) n_{\mathrm{low}\omega_j}\right\} \quad (47)$$

$$\frac{dn_{\mathrm{low}0}}{dt} = -\gamma_{\mathrm{low}0}\left(n_{\mathrm{low}0} - \frac{\kappa_{\mathrm{seed}}(t)}{\gamma_{\mathrm{low}0}}\right) + G_{\mathrm{up}0} n_{\mathrm{upP}}\left(n_{\mathrm{low}0} + 1\right) + G_{\mathrm{low}0} n_{\mathrm{lowP}}\left(n_{\mathrm{low}0} + 1\right) + \\ + \sum_{j=1}^{N}\left\{\gamma_{\mathrm{low}}^{0\omega_j}\left(n_{\mathrm{low}0} + 1\right) n_{\mathrm{low}\omega_j} - \gamma_{\mathrm{low}}^{\omega_j 0}\left(n_{\mathrm{low}\omega_j} + D_{\omega_j}\right) n_{\mathrm{low}0}\right\} \quad (48)$$

where we denote

$$G_{\mathrm{up}\omega_j} = \frac{\left(g\cos\varphi_{\mathrm{P}}\sin\varphi_{\omega_j}\right)^2\left(\gamma_{\mathrm{upP}} + \gamma_{\mathrm{low}\omega_j} + \gamma_{\mathrm{vib}}\right)}{\left(\omega_{\mathrm{upP}} - \omega_{\mathrm{low}\omega_j} - \omega_{\mathrm{vib}}\right)^2 + \frac{1}{4}\left(\gamma_{\mathrm{upP}} + \gamma_{\mathrm{low}\omega_j} + \gamma_{\mathrm{vib}}\right)^2} \quad (49)$$

$$G_{\mathrm{up}0} = \frac{\left(g\cos\varphi_{\mathrm{P}}\sin\varphi_{0}\right)^2\left(\gamma_{\mathrm{upP}} + \gamma_{\mathrm{low}0} + \gamma_{\mathrm{vib}}\right)}{\left(\omega_{\mathrm{upP}} - \omega_{\mathrm{low}0} - \omega_{\mathrm{vib}}\right)^2 + \frac{1}{4}\left(\gamma_{\mathrm{upP}} + \gamma_{\mathrm{low}0} + \gamma_{\mathrm{vib}}\right)^2} \quad (50)$$

$$G_{\mathrm{low}\omega_j} = \frac{\left(g\sin\varphi_{\mathrm{P}}\sin\varphi_{\omega_j}\right)^2\left(\gamma_{\mathrm{lowP}} + \gamma_{\mathrm{low}\omega_j} + \gamma_{\mathrm{vib}}\right)}{\left(\omega_{\mathrm{lowP}} - \omega_{\mathrm{low}\omega_j} - \omega_{\mathrm{vib}}\right)^2 + \frac{1}{4}\left(\gamma_{\mathrm{lowP}} + \gamma_{\mathrm{low}\omega_j} + \gamma_{\mathrm{vib}}\right)^2} \quad (51)$$

$$G_{\mathrm{low}0} = \frac{\left(g\sin\varphi_{\mathrm{P}}\sin\varphi_{0}\right)^2\left(\gamma_{\mathrm{lowP}} + \gamma_{\mathrm{low}0} + \gamma_{\mathrm{vib}}\right)}{\left(\omega_{\mathrm{lowP}} - \omega_{\mathrm{low}0} - \omega_{\mathrm{vib}}\right)^2 + \frac{1}{4}\left(\gamma_{\mathrm{lowP}} + \gamma_{\mathrm{low}0} + \gamma_{\mathrm{vib}}\right)^2} \quad (52)$$

where $j = 1, ..., N$.

We use the quantum regression theorem to calculate the emission spectrum from the lower polariton branch. To do this, first we obtain the equations for the amplitudes of lower polaritons, $s_{\mathrm{low}\mathbf{k}} = \langle\hat{s}_{\mathrm{low}\mathbf{k}}\rangle$, and vibrons, $b_{\mathbf{q}} = \left\langle\hat{b}_{\mathbf{q}}\right\rangle$ from the master equation (1)

$$\frac{ds_{\mathrm{low}\mathbf{k}}}{dt} = -i\omega_{\mathrm{low}\mathbf{k}} s_{\mathrm{low}\mathbf{k}} - \frac{1}{2}\gamma_{\mathrm{low}\mathbf{k}} s_{\mathrm{low}\mathbf{k}} + \frac{1}{2}\sum_{\mathbf{k}'}\left(\gamma_{\mathrm{low}}^{\mathbf{k}\mathbf{k}'}|s_{\mathrm{low}\mathbf{k}'}|^2 - \gamma_{\mathrm{low}}^{\mathbf{k}'\mathbf{k}}\left(1 + |s_{\mathrm{low}\mathbf{k}'}|^2\right)\right) s_{\mathrm{low}\mathbf{k}} \\ + ig\cos\varphi_{\mathbf{k}_{\mathrm{pump}}}\sin\varphi_{\mathbf{k}} s_{\mathrm{up}\mathbf{k}_{\mathrm{pump}}} b^*_{\mathbf{k}_{\mathrm{pump}}-\mathbf{k}} + ig\sin\varphi_{\mathbf{k}_{\mathrm{ex}}}\sin\varphi_{\mathbf{k}} s_{\mathrm{low}\mathbf{k}_{\mathrm{pump}}} b^*_{\mathbf{k}_{\mathrm{pump}}-\mathbf{k}} \quad (53)$$

$$\frac{db_{\mathbf{k}_{\mathrm{pump}}-\mathbf{k}}}{dt} = -i\omega_{\mathrm{vib}} b_{\mathbf{k}_{\mathrm{pump}}-\mathbf{k}} - \frac{1}{2}\gamma_{\mathrm{vib}} b_{\mathbf{k}_{\mathrm{pump}}-\mathbf{k}} + \\ + ig\cos\varphi_{\mathbf{k}_{\mathrm{pump}}}\sin\varphi_{\mathbf{k}} s_{\mathrm{up}\mathbf{k}_{\mathrm{pump}}} s^*_{\mathrm{low}\mathbf{k}} + ig\sin\varphi_{\mathbf{k}_{\mathrm{pump}}}\sin\varphi_{\mathbf{k}} s_{\mathrm{low}\mathbf{k}_{\mathrm{pump}}} s^*_{\mathrm{low}\mathbf{k}} \quad (54)$$

The quality factor of vibron modes in MeLPPP is approximately 100 as follows from the Raman spectrum of the bare MeLPPP film represented in Fig. S2. This value is much smaller (factor of six) then the quality factor of the cavity. Therefore we can exclude the amplitude of vibrons

$$b^*_{\mathbf{k}_{\rm pump}-\mathbf{k}} \approx -\frac{g\cos\varphi_{\mathbf{k}_{\rm pump}}\sin\varphi_{\mathbf{k}}}{\omega_{{\rm up}\mathbf{k}_{\rm pump}}-\omega_{{\rm low}\mathbf{k}}-\omega_{\rm vib}-i\gamma_{\rm vib}/2}s^*_{{\rm up}\mathbf{k}_{\rm pump}}s_{{\rm low}\mathbf{k}}- \\ -\frac{g\sin\varphi_{\mathbf{k}_{\rm pump}}\sin\varphi_{\mathbf{k}}}{\omega_{{\rm low}\mathbf{k}_{\rm pump}}-\omega_{{\rm low}\mathbf{k}}-\omega_{\rm vib}-i\gamma_{\rm vib}/2}s^*_{{\rm low}\mathbf{k}_{\rm pump}}s_{{\rm low}\mathbf{k}} \quad (55)$$

and obtain the equation for the amplitudes of the lower polaritons

$$\frac{ds_{{\rm low}\mathbf{k}}}{dt} = -i\omega_{{\rm low}\mathbf{k}}s_{{\rm low}\mathbf{k}} - \frac{1}{2}\gamma_{{\rm low}\mathbf{k}}s_{{\rm low}\mathbf{k}} + \frac{1}{2}\sum_{\mathbf{k}'}\left(\gamma^{\mathbf{k}\mathbf{k}'}_{\rm low}|s_{{\rm low}\mathbf{k}'}|^2 - \gamma^{\mathbf{k}'\mathbf{k}}_{\rm low}\left(1+|s_{{\rm low}\mathbf{k}'}|^2\right)\right)s_{{\rm low}\mathbf{k}}- \\ -i\frac{\left(g\cos\varphi_{\mathbf{k}_{\rm pump}}\sin\varphi_{\mathbf{k}}\right)^2}{\omega_{{\rm up}\mathbf{k}_{\rm pump}}-\omega_{{\rm low}\mathbf{k}}-\omega_{\rm vib}-i\gamma_{\rm vib}/2}\left|s_{{\rm up}\mathbf{k}_{\rm eump}}\right|^2 s_{{\rm low}\mathbf{k}} \\ -i\frac{\left(g\sin\varphi_{\mathbf{k}_{\rm pump}}\sin\varphi_{\mathbf{k}}\right)^2}{\omega_{{\rm low}\mathbf{k}_{\rm pump}}-\omega_{{\rm low}\mathbf{k}}-\omega_{\rm vib}-i\gamma_{\rm vib}/2}\left|s_{{\rm low}\mathbf{k}_{\rm pump}}\right|^2 s_{{\rm low}\mathbf{k}} \quad (56)$$

Applying the quantum regression theorem to equation (56) we obtain the equation for the correlators $\left\langle \hat{s}^\dagger_{{\rm low}\mathbf{k}}(t+\tau)\,\hat{s}_{{\rm low}\mathbf{k}}(t)\right\rangle$

$$\frac{d\left\langle \hat{s}^\dagger_{{\rm low}\mathbf{k}}(t+\tau)\,\hat{s}_{{\rm low}\mathbf{k}}(t)\right\rangle}{d\tau} = i\omega_{{\rm low}\mathbf{k}}\left\langle \hat{s}^\dagger_{{\rm low}\mathbf{k}}(t+\tau)\,\hat{s}_{{\rm low}\mathbf{k}}(t)\right\rangle - \frac{1}{2}\gamma_{{\rm low}\mathbf{k}}\left\langle \hat{s}^\dagger_{{\rm low}\mathbf{k}}(t+\tau)\,\hat{s}_{{\rm low}\mathbf{k}}(t)\right\rangle \\ +\frac{1}{2}\sum_{\mathbf{k}'}\left(\gamma^{\mathbf{k}\mathbf{k}'}_{\rm low}n_{{\rm low}\mathbf{k}'}(t) - \gamma^{\mathbf{k}'\mathbf{k}}_{\rm low}\left(1+n_{{\rm low}\mathbf{k}'}(t)\right)\right)\left\langle \hat{s}^\dagger_{{\rm low}\mathbf{k}}(t+\tau)\,\hat{s}_{{\rm low}\mathbf{k}}(t)\right\rangle + \\ +i\left[\frac{\left(g\cos\varphi_{\mathbf{k}_{\rm pump}}\sin\varphi_{\mathbf{k}}\right)^2 n_{{\rm up}\mathbf{k}_{\rm pump}}(t)}{\omega_{{\rm up}\mathbf{k}_{\rm pump}}-\omega_{{\rm low}\mathbf{k}}-\omega_{\rm vib}+i\gamma_{\rm vib}/2} + \frac{\left(g\sin\varphi_{\mathbf{k}_{\rm pump}}\sin\varphi_{\mathbf{k}}\right)^2 n_{{\rm low}\mathbf{k}_{\rm pump}}(t)}{\omega_{{\rm low}\mathbf{k}_{\rm pump}}-\omega_{{\rm low}\mathbf{k}}-\omega_{\rm vib}+i\gamma_{\rm vib}/2}\right]\left\langle \hat{s}^\dagger_{{\rm low}\mathbf{k}}(t+\tau)\,\hat{s}_{{\rm low}\mathbf{k}}(t)\right\rangle \quad (57)$$

with initial condition $\left\langle \hat{s}^\dagger_{{\rm low}\mathbf{k}}(t)\,\hat{s}_{{\rm low}\mathbf{k}}(t)\right\rangle = n_{{\rm low}\mathbf{k}}(t)$

To discretize the equation for the correlators $\left\langle \hat{s}^\dagger_{{\rm low}\mathbf{k}}(t+\tau)\,\hat{s}_{{\rm low}\mathbf{k}}(t)\right\rangle$ we use

$$\left\langle \hat{s}^\dagger_{{\rm low}\omega_j}(t+\tau)\,\hat{s}_{{\rm low}\omega_j}(t)\right\rangle = \sum_{\mathbf{k},\ \omega_j-\delta\omega<\omega_{{\rm low}\mathbf{k}'}<\omega_j}\left\langle \hat{s}^\dagger_{{\rm low}\mathbf{k}}(t+\tau)\,\hat{s}_{{\rm low}\mathbf{k}}(t)\right\rangle \quad (58)$$

$$\left\langle \hat{s}^\dagger_{{\rm low}0}(t+\tau)\,\hat{s}_{{\rm low}0}(t)\right\rangle = \left\langle \hat{s}^\dagger_{{\rm low}\mathbf{k}=0}(t+\tau)\,\hat{s}_{{\rm low}\mathbf{k}=0}(t)\right\rangle \quad (59)$$

where $j = 1,..,N$.

As a result we obtain

$$\frac{d\left\langle \hat{s}^{\dagger}_{\mathrm{low}\omega_j}\left(t+\tau\right)\hat{s}_{\mathrm{low}\omega_j}\left(t\right)\right\rangle}{d\tau}=\left(i\omega_{\mathrm{low}\omega_j}-\frac{1}{2}\gamma_{\mathrm{low}\omega_j}\right)\left\langle \hat{s}^{\dagger}_{\mathrm{low}\omega_j}\left(t+\tau\right)\hat{s}_{\mathrm{low}\omega_j}\left(t\right)\right\rangle$$
$$+\frac{1}{2}\sum_{m=1}^{N}\left(\gamma_{\mathrm{low}}^{\omega_j\omega_m}n_{\mathrm{low}\omega_m}\left(t+\tau\right)-\gamma_{\mathrm{low}}^{\omega_m\omega_j}\left(D_{\omega_m}+n_{\mathrm{low}\omega_m}\left(t+\tau\right)\right)\right)\left\langle \hat{s}^{\dagger}_{\mathrm{low}\omega_j}\left(t+\tau\right)\hat{s}_{\mathrm{low}\omega_j}\left(t\right)\right\rangle+$$
$$+\frac{1}{2}\left(\gamma_{\mathrm{low}}^{\omega_j 0}n_{\mathrm{low}0}\left(t+\tau\right)-\gamma_{\mathrm{low}}^{0\omega_j}\left(1+n_{\mathrm{low}0}\left(t+\tau\right)\right)\right)\left\langle \hat{s}^{\dagger}_{\mathrm{low}\omega_j}\left(t+\tau\right)\hat{s}_{\mathrm{low}\omega_j}\left(t\right)\right\rangle+$$
$$+i\left[\frac{\left(g\cos\varphi_{\mathrm{P}}\sin\varphi_{\omega_j}\right)^2 n_{\mathrm{upP}}\left(t+\tau\right)}{\omega_{\mathrm{upP}}-\omega_{\mathrm{low}\omega_j}-\omega_{\mathrm{vib}}+i\gamma_{\mathrm{vib}}/2}+\frac{\left(g\sin\varphi_{\mathrm{P}}\sin\varphi_{\omega_j}\right)^2 n_{\mathrm{lowP}}\left(t+\tau\right)}{\omega_{\mathrm{lowP}}-\omega_{\mathrm{low}\omega_j}-\omega_{\mathrm{vib}}+i\gamma_{\mathrm{vib}}/2}\right]\left\langle \hat{s}^{\dagger}_{\mathrm{low}\omega_j}\left(t+\tau\right)\hat{s}_{\mathrm{low}\omega_j}\left(t\right)\right\rangle \tag{60}$$

$$\frac{d\left\langle \hat{s}^{\dagger}_{\mathrm{low}0}\left(t+\tau\right)\hat{s}_{\mathrm{low}0}\left(t\right)\right\rangle}{d\tau}=\left(i\omega_{\mathrm{low}0}-\frac{1}{2}\gamma_{\mathrm{low}0}\right)\left\langle \hat{s}^{\dagger}_{\mathrm{low}0}\left(t+\tau\right)\hat{s}_{\mathrm{low}0}\left(t\right)\right\rangle$$
$$+\frac{1}{2}\sum_{j=1}^{N}\left(\gamma_{\mathrm{low}}^{0\omega_j}n_{\mathrm{low}\omega_j}\left(t+\tau\right)-\gamma_{\mathrm{low}}^{\omega_j 0}\left(D_{\omega_j}+n_{\mathrm{low}\omega_j}\left(t+\tau\right)\right)\right)\left\langle \hat{s}^{\dagger}_{\mathrm{low}0}\left(t+\tau\right)\hat{s}_{\mathrm{low}0}\left(t\right)\right\rangle+$$
$$+i\left[\frac{\left(g\cos\varphi_{\mathrm{P}}\sin\varphi_0\right)^2 n_{\mathrm{upP}}\left(t+\tau\right)}{\omega_{\mathrm{upP}}-\omega_{\mathrm{low}0}-\omega_{\mathrm{vib}}+i\gamma_{\mathrm{vib}}/2}+\frac{\left(g\sin\varphi_{\mathrm{P}}\sin\varphi_0\right)^2 n_{\mathrm{lowP}}\left(t+\tau\right)}{\omega_{\mathrm{lowP}}-\omega_{\mathrm{low}0}-\omega_{\mathrm{vib}}+i\gamma_{\mathrm{vib}}/2}\right]\left\langle \hat{s}^{\dagger}_{\mathrm{low}0}\left(t+\tau\right)\hat{s}_{\mathrm{low}0}\left(t\right)\right\rangle \tag{61}$$

where $j=1,...,N$. In these equations the functions $n_{\mathrm{upP}}\left(t+\tau\right)$, $n_{\mathrm{lowP}}\left(t+\tau\right)$, $n_{\mathrm{low}\omega_j}\left(t+\tau\right)$ and $n_{\mathrm{low}0}\left(t+\tau\right)$ are known from solution of the equations (45)-(48).

The emission spectrum from the lower polarion branch can be calculated from two time correlation functions $\left\langle \hat{s}^{\dagger}_{\mathrm{low}\omega_j}\left(t+\tau\right)\hat{s}_{\mathrm{low}\omega_j}\left(t\right)\right\rangle$ and $\left\langle \hat{s}^{\dagger}_{\mathrm{low}0}\left(t+\tau\right)\hat{s}_{\mathrm{low}0}\left(t\right)\right\rangle$ according to

$$S_0\left(\omega\right)=\mathrm{Re}\int_0^{+\infty}\left\langle \hat{s}^{\dagger}_{\mathrm{low}0}\left(t+\tau\right)\hat{s}_{\mathrm{low}0}\left(t\right)\right\rangle e^{-i\omega\tau}d\tau \tag{62}$$

$$S_{\omega_j}\left(\omega\right)=\mathrm{Re}\int_0^{+\infty}\left\langle \hat{s}^{\dagger}_{\mathrm{low}\omega_j}\left(t+\tau\right)\hat{s}_{\mathrm{low}\omega_j}\left(t\right)\right\rangle e^{-i\omega\tau}d\tau \tag{63}$$

IV. NUMERICAL SIMULATIONS

We generate the system of differential equations based on Eqs. (45)-(48) consisting of the modes in upper and lower polariton branches at $\mathbf{k}_{\mathrm{pump}}$, the most intense vibron mode with

energy equals to $\omega_{\text{vib}} = 0.199$ eV and the set of equidistant $N = 120$ modes in frequency space that fill the bottom of the lower polariton dispersion within the momentum range of $[|k_{\text{min}}| = 0\ \mu\text{m}^{-1}, |\text{k}_{\text{max}}| = 2\ \mu\text{m}^{-1}]$. All the modes are shown in Fig. S5 as green dots on top of the polariton dispersion relations. Modes at the bottom of the lower polariton branch are shown in the inset of Fig. S5.

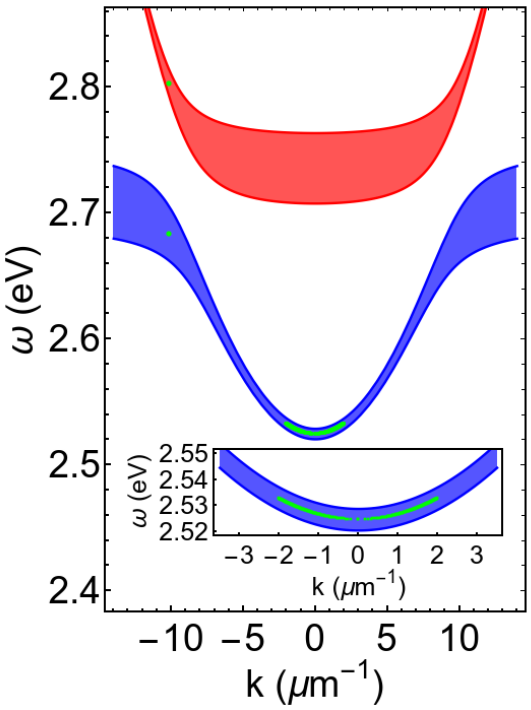

FIG. S5. The dispersion of the lower (blue) and upper (red) polariton branches. The width of the lines along the frequency axes indicates the FWHM of the polaritons, which is corresponds to the dissipation rate. The discrete modes are shown as green dots.

To calculate polariton dispersion relations we use the standard parabolic dispersion of the cavity $\omega_{\text{cav}\mathbf{k}} = \omega_{\text{cav}0} + \alpha_{\text{cav}} \cdot \mathbf{k}^2$, where the cut-off frequency at $\mathbf{k} = 0$ is equal to $\omega_{\text{cav}0} = 2.54$ eV and the curvature parameter $\alpha_{\text{cav}} = 2.2$ meVμm^2 is obtained from experimental data in Fig. S1a. In turn, Frenkel excitons are well-known as dispersionless particles, therefore it is reasonable to assume the constant energy of $\omega_{\text{exc}} = 2.72$ eV. Similarly, the coupling constant between exciton and cavity modes is fixed at $\Omega_{\text{R}\mathbf{k}} = 55$ meV, regardless of the in-plane quasimomentum $\mathbf{k}$. The photon decay and effective exciton dephasing rates (including inhomogeneous broadening) are assumed to be $\mathbf{k}$-independent values $\gamma_{\text{cav}\mathbf{k}} = 4.2$ meV and $\gamma_{\text{exc}} = 60$ meV respectively. The photon decay time is obtained from the measured quality

factor of empty cavities ($Q = 600$). The effective exciton dephasing time is assessed from the linewidth of the inhomogeneously broadened electronic $S_{0,0} \rightarrow S_{1,0}$ singlet transition of the MeLPPP bare film.

Finally, we use Eqs. (17)-(18) to plot lower and upper polariton branches in Fig. S5, where the linewidth for both dependencies correspond to dissipation rate of the lower $\gamma_{\mathrm{low}\mathbf{k}} = \gamma_{\mathrm{cav}\mathbf{k}} \cos^2 \phi_{\mathbf{k}} + \gamma_{\mathrm{exc}} \sin^2 \phi_{\mathbf{k}}$ and upper $\gamma_{\mathrm{up}\mathbf{k}} = \gamma_{\mathrm{cav}\mathbf{k}} \sin^2 \phi_{\mathbf{k}} + \gamma_{\mathrm{exc}} \cos^2 \phi_{\mathbf{k}}$ polaritons, respectively.

The incident angle of the pump beam is $\theta = 45^{\mathrm{o}}$ which corresponds to in-plane momentum $\hbar \mathbf{k}_{\mathrm{pump}} = 10\ \mu\mathrm{m}^{-1}$. The pump pulse duration of 150 fs corresponds to $t_{\mathrm{pump}} = 2\pi \cdot 30\ \mathrm{eV}^{-1}$. Exciton-vibron interaction constant g is left as variable parameter during numerical simulations. We get the best fit results with $g = 0.2$ meV. The value agrees well with the experimental one assessed independently using a cross-section of Raman scattering [10] and the theoretical approach developed in Ref. [14].

To study dynamics of the polariton condensation and associated nonlinear emission from the organic microcavity we set the thermalization rate for the lower polaritons at the level of $\gamma_{\mathrm{low}}^{\mathbf{k_1}\mathbf{k_2}} = 10^{-7}$ eV (it corresponds to the best fit result) for $\omega_{\mathrm{low}\mathbf{k_1}} < \omega_{\mathrm{low}\mathbf{k_2}}$ and use the thermal energy $k_B T = 0.025$ eV corresponding room temperature 300 K. The vibron dissipation rate is estimated from the Raman spectrum of MeLPPP $\gamma_{\mathrm{vib}} = 0.0025$ eV. Following experimental conditions we choose $|k| < 0.2\ \mu\mathrm{m}^{-1}$. The seed pulse duration of 200 fs corresponds to $t_{\mathrm{seed}} = 2\pi \cdot 40\ \mathrm{eV}^{-1}$. Finally, we apply the following initial conditions to the system: $n_{\mathrm{upP}}(0) = 0$, $n_{\mathrm{lowP}}(0) = 0$, $n_{\mathrm{low0}}(0) = 0$, $n_{\mathrm{low}\omega_j}(0) = 0$ for $j = 1, ..., N$.

We run numerical simulations of spontaneously-formed polariton condensation to understand the formation of the condensed state. Fig.S6 shows time-integrated polariton population $\langle n \rangle$ across the lower polariton eigenstates as a function of dimensionless pump intensity P. Importantly, the population exponentially decreases with increasing polariton eigenstate energy below the condensation threshold without any change in the slope of the exponent, according to Boltzmann distribution of the thermal polariton gas. However, above the threshold, it exhibits accumulation of polariton population at the ground and nearby energy states due to bosonic stimulation followed by the formation of the non-equilibrium Bose-Einstein condensate.

The integrated polariton density in the vicinity of the ground state as a function of pump (Fig. S7a. black) demonstrates a S-shape dependence in agreement with the previous reports on the BEC formation at room-temperature [1]. The integration takes place within ± 0.2

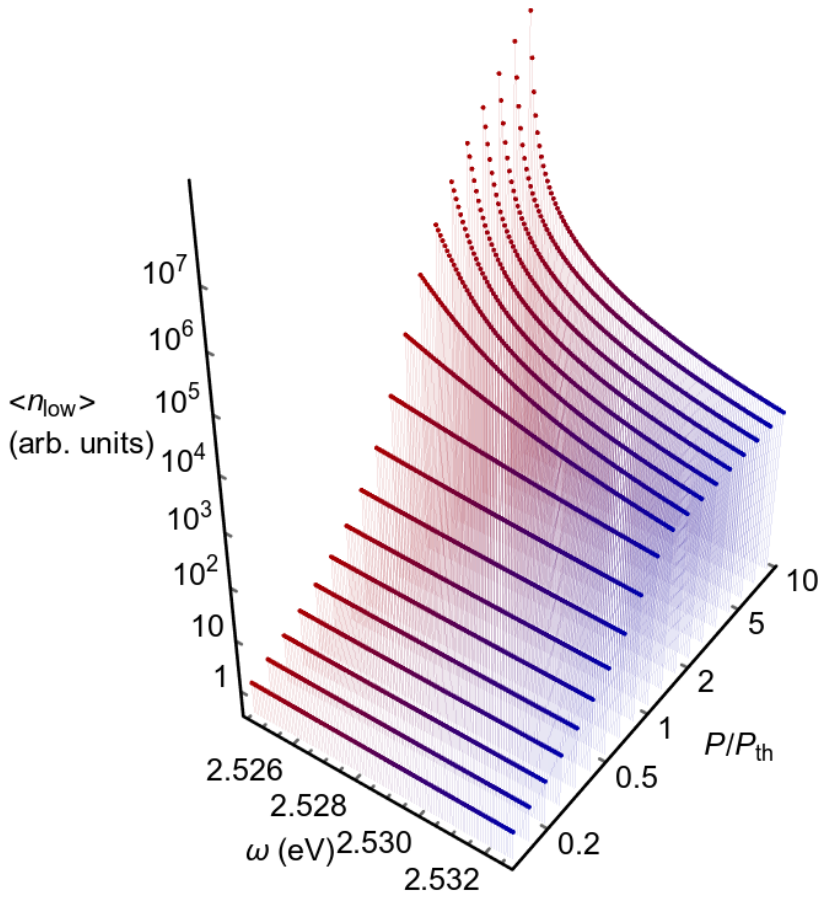

FIG. S6. Time-integrated polariton population $\langle n \rangle$ at different energy states ω as a function of dimensionless pump intensity P.

μm^{-1} according to the experimental configurations. Here we also plot the result of numerical simulations for the seeded condensate (Fig. S7a. red). One can see remarkable agreement with the experimental curves represented in Fig. 1b of the main text. Importantly, our model adequately describes polariton population distribution in *(E,k)*-space. Fig. S7b and c demonstrate spontaneously formed and seeded condensates respectively at the incident pump fluence of $P \sim 2P_{th}$. Here we use the seed pulse carrying 1000 photons that resonantly injects polaritons into the ground state. As we form macroscopic occupation of the ground state at the very initial stage of polariton condensation, it boosts relaxation towards the ground state through the vibron-assisted bosonic stimulation. One can see the predominant population into the pre-occupied states via the sharp distribution of the polariton population along the lower branch. Both simulations accurately describe experimental *(E,k)* distributions from Fig. 1b,c of the main manuscript as well as contrast dependence on the seed energy.

Note that theory predicts 11% contrast at the single photon level. In fact, it manifests our microscopic theory is adequate describing physical mechanisms underlying vibron-mediated polariton condensation in the organic system at resonant excitation and seeding.

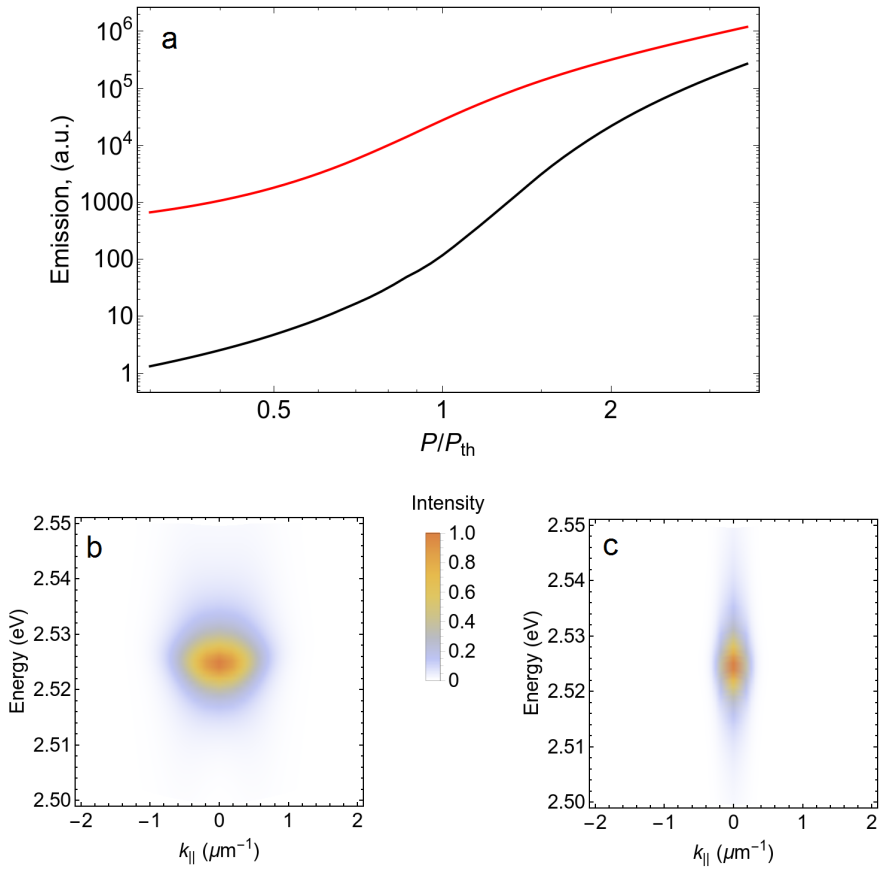

FIG. S7. **a**, Emission of the seeded (red) and spontaneously formed (black condensates integrated over the polariton state within ± 0.2 μm^{-1} momentum range as a function of pump intensity P. **b** and **c**, Time-integrated energy, momentum *(E,k)*-distribution of polariton population along the lower branch for the spontaneously formed and seeded polariton condensates respectively. Population distributions are simulated at $P = 2P_{\text{th}}$

To peek behind the curtain of the extraordinary nonlinear response of the system, we examine switching contrast defined in the main manuscript as $Contrast = \frac{P_{\text{seed}}}{P_{\text{spont}}} - 1$ under different exciton-photon (Ω_{R}) and exciton-vibron (g) coupling constants. Figure S8 shows the contrast of switching under $\langle n \rangle = 10$ seed photons as a function of coupling constants. In both cases the contrast depends sub-linearly on g and Ω_{R}

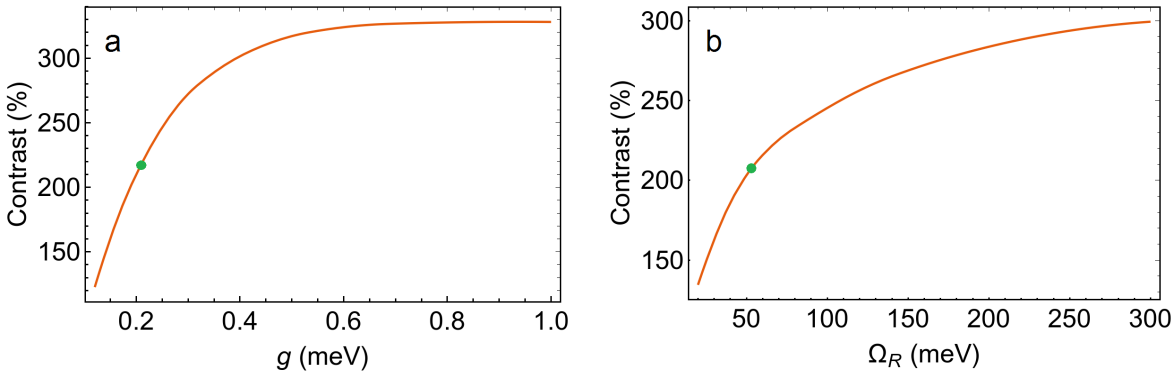

FIG. S8. **a**, The switching contrast as a function of exciton-vibron coupling (g) with the fixed exciton-photon coupling $\Omega_{\mathrm{R}} = 55$ meV. **b**, The switching contrast as a function of exciton-photon coupling (Ω_{R}) with the fixed exciton-vibron coupling $g = 0.2$ meV. All simulations are done at the fixed pump fluence of $P = 2P_{\mathrm{th}}$. Contrast is obtained by integration E,k distributions over the ground state momentum range of $\pm 0.2\ \mu\mathrm{m}^{-1}$

With increasing exciton-photon and exciton-vibron interactions we observe further increase in contrast values followed by saturation regime. The increase of contrast is a quite intuitive result since both exciton-photon and exciton-vibron coupling terms in the Hamiltonian Eq.(12)-(7) favor stimulated polariton relaxation from higher energy excited states towards the ground state. Further increase of the coupling constants does not improve switching contrast as the bosonic stimulation is already strong enough to form a polariton condensate. The highly nonlinear dynamics of the process saturates the polariton population at finite times in this regime.

V. STATISTICAL ANALYSIS OF SINGLE-PHOTON SWITCHING

In the following, we present a detailed statistical analysis of single-shot measurements that provide direct evidence of single-photon switching at $\langle n \rangle = 1$. Let us consider the probability of having 0, 1, 2 etc photons in a seed pulse. It is described by the probability density function (PDF) of the Poisson distribution according to the pulse of the seed beam expressed for an average photon number $\langle n \rangle$. Fig. S9 shows the probability for $\langle n \rangle = 9.3$, 2.7, 1 considered above and focus in the case of $\langle n \rangle = 1$ that is of utmost importance here. One can see that roughly 92% of the seed pulses contain either one or two photons or no

photons at all. Only 8% of pulses have $n \geq 3$ photons.

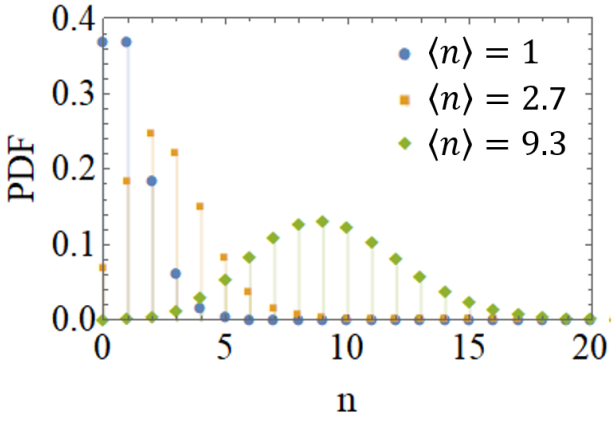

FIG. S9. Probability density function (PDF) of Poisson distribution with an average value $\langle n \rangle$ equals to 1 (blue), 2.7 (orange) and 9.3 (green).

Next, we drop the 8% of high photon number realisations from the histogram. Since the actual distribution of the total polariton population seeded with $n \geq 3$ photons is not accessible, we assume the worst-case scenario and remove the top 8% of polariton populations. Fig. S10 shows the histogram of the truncated data. Transparent bars at the high population tail of the histogram correspond to the 72 single condensate realisations that we removed (8% of 900 shots).

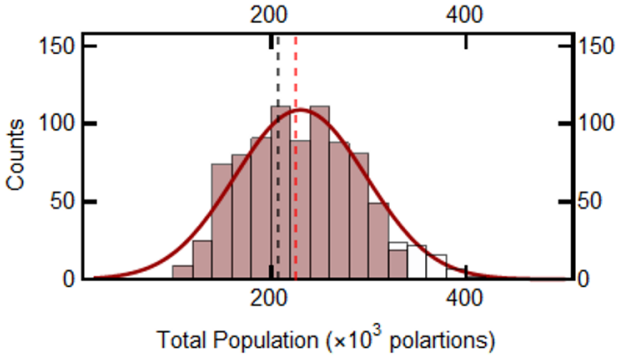

FIG. S10. Truncated histogram of total polariton population of the condensates seeded with $\langle n \rangle = 1$ photons on average. Red dashed line shows the mean value of the truncated data, black dashed line corresponds to the peak in the distribution of spontaneously formed condensates. The solid red line is the Gaussian fit of the initial data.

The average total population of the condensate seeded with one and two photon states

is equal to 225.2 against 207.2 ($\times 10^3$ polaritons) for the spontaneously formed condensates leading to the contrast of 8.7%. Considering the truncated data still contains 40% of empty realizations when there is not any photon in a seed pulse, the contrast for one/two-photon switching becomes 14.5%. This number should be understood as the lower limit of the switching contrast as it relies on the worst-case scenario wherein 8% of seed pulses with $n \geq 3$ photons accounts for the top 8% of the total population distribution. In order to obtain a similar picture for 0- and 1-photon events only (50% realizations are single-photon events, another half is empty) we remove the next 166 realizations in the high population tail of the histogram. Fig. S11 shows the histogram truncated at the level of 26.4% from the top population values.

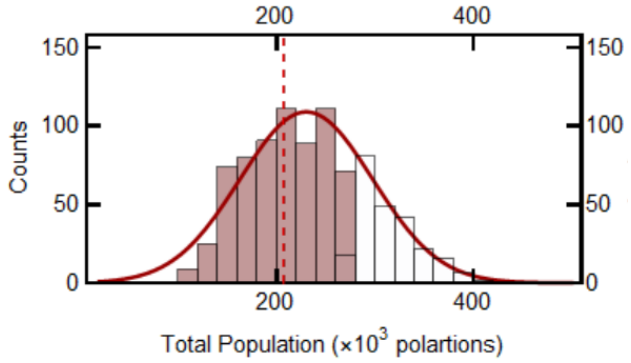

FIG. S11. Truncated histogram of total polariton population of the condensates seeded with $\langle n \rangle = 1$ photons on average. Red dashed line shows the mean value of the truncated data, black dashed line corresponds to the peak in the distribution of spontaneously formed condensates. The solid red line is the Gaussian fit of the initial data.

Although this approach obviously gives non-physical distribution of condensate realisations, the stringent statistical truncation supports our claim of single-photon switching (i.e. $Contrast > 0$) but does not enable for a proper discrimination between one- and two-photon contributions. To overcome this problem one should apply a reasonable sampling rule to select realisations according to total population distributions of the condensate seeded by 2-,3-,4- etc photon states. Although, we cannot extract this information from the data shown in Fig. 4e of the main text, we have recorded the population distribution of the spontaneously formed condensates. We apply the distribution function of the spontaneously formed condensates on the statistical distribution we obtained in the presence of the seed and randomly sample occurrences to investigate whether or not there is a statistical dif-

ference between spontaneous condensation and one photon seeded condensation. Following this approach, we randomly sample 662 condensate realisations (73.6% of 900 shots) from the experimental data represented in Fig. 4e according to the population distribution of the spontaneously formed condensate. By imposing the distribution of the spontaneously formed condensates on the seeded results allows us to reasonably exclude multi-photon events, i.e. such sampling statistically corresponds to single-photon and empty events only. To ensure the contrast is free from any effects of biased choices we take 12 random samplings of both: spontaneous and seeded condensate realisations. The result of 12 random samplings is shown in Fig. S12, where black and red histograms correspond to the spontaneously formed and seeded condensates.

In all sampling sets we observe a clear change in average total population upon seeding with the single-photon state as indicated by red and black vertical dashed lines. The average population of the spontaneous and seeded condensates appears to be equal 209.5 ± 1.2 and 220 ± 1.1 ($\times 10^3$ polaritons) as shown in Fig. S13 by black and red points respectively.

Taking into account that half of each sampling set contains empty events, i.e. no photons in the seed pulse, we arrive at single-photon switching contrast of 10%. This value is fully consistent with the overall contrast for $\langle n \rangle = 1$ equal to 11% used in the manuscript. In fact, all 900 shots contains 36.8% -empty events, 36.8% - single-photon events with contrast 10%, 26.4% - two-photon events, etc with cumulative contrast 28% defined from experimental data for $\langle n \rangle = 2.7$, where 6.7% of empty events have been taken into account (see Poissonian distribution in Fig. S9. From the statistical analysis presented above, we derive single-photon switching contrast of 10%, ratifying our claim of single-photon switching.

Although in Fig. 4e of the main text we demonstrate the contrast at the single-photon level by means of averaging over 300 single shots in each measurement, the number of single shots to observe switching with high fidelity could be further squeezed down to 30 shots as shown in Fig. S14.

In Fig. S14 we plot mean total polariton population averaged over 30 (a) and 100 (b) randomly sampled single condensate realizations from the data set in Fig. 4e of the main text. Analysis of the data averaged over 30 shots reveals single-photon switching with contrast of 11% and high fidelity of 90% that to the best of our knowledge outperforms the existing platforms in terms of statistics required for single-photon switching. Moreover, being averaged over 100 shots (Fig. S14b) the device demonstrate fully deterministic switching

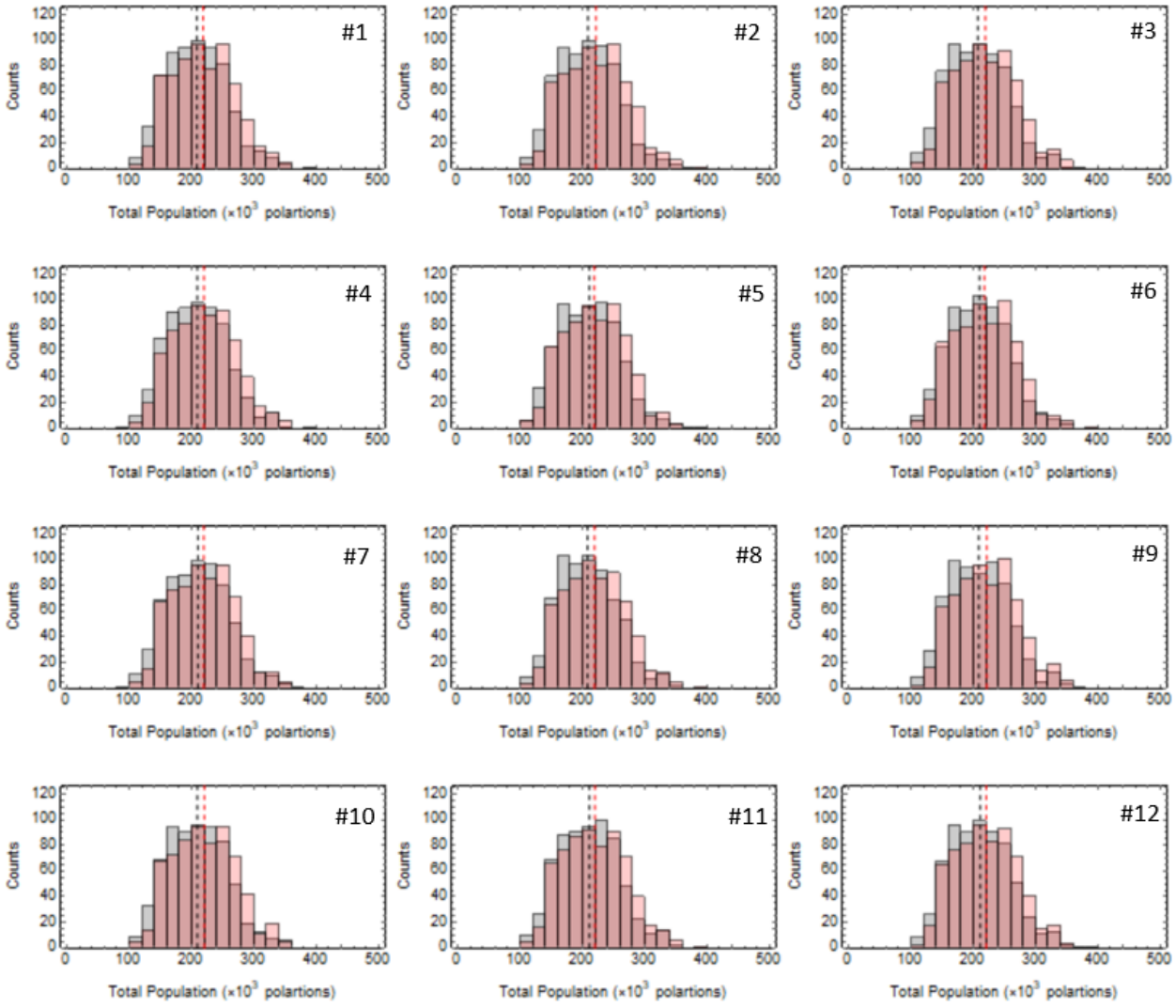

FIG. S12. Histograms of 12 samplings obtained by randomly picking 662 single shots out of 900 initial realizations according to the total population distribution of the spontaneously formed condensate. Red bars correspond to the seeded condensate, black to the spontaneously formed one. Black and red dashed lines indicate the mean total population for the spontaneously formed and seeded polariton condensate respectively.

capabilities holding a promise for deterministic single shot switching, discussed in the next section.

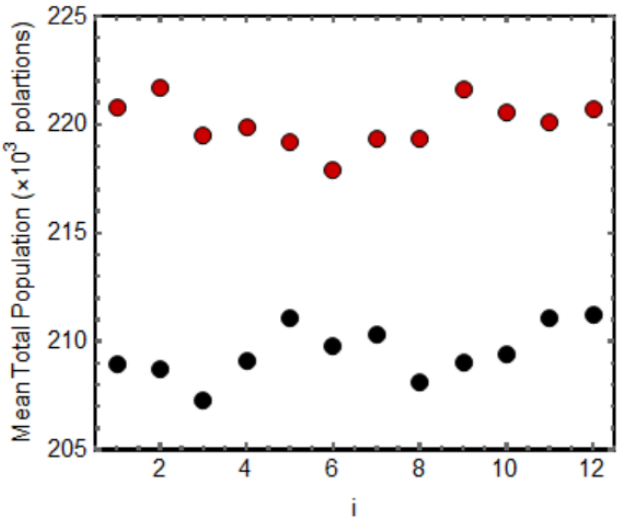

FIG. S13. Mean total population of the spontaneously formed (black) and seeded polariton condensates (red), where i is the sampling number from Fig. S12.

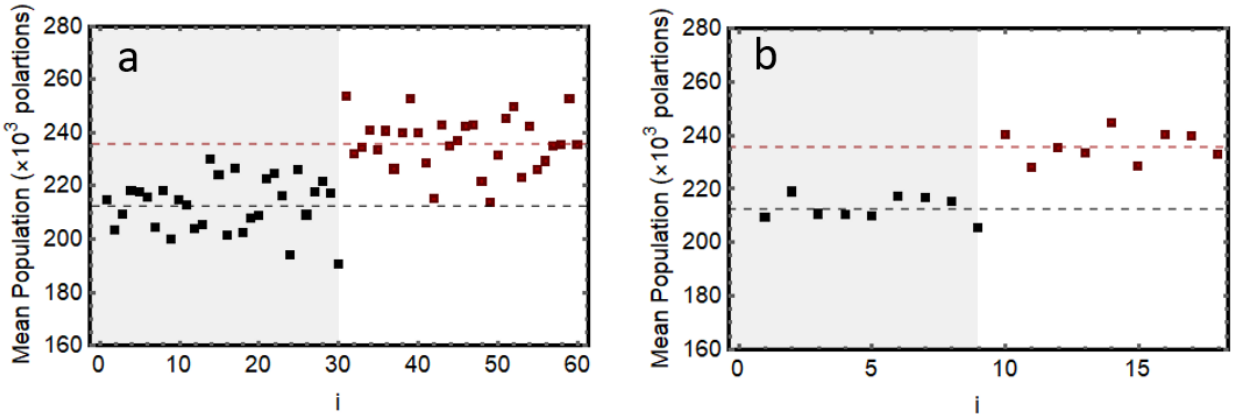

FIG. S14. Mean total polariton population of spontaneously-formed (black dots, grey-shaded area) and seeded condensate at the single-photon level (red dots) averaged over 30 **a**, and 100 **b** single shot realizations.

VI. OPTIMIZING THE CONTRAST OF THE SINGLE-PHOTON SWITCH

Although we have optimized our experimental arrangements to maximize the effect of single-photon switching, there is still plenty of room for further improvements within the rich parameter space of our system. There are several strategies to deal with it, one can either fight the noise or boost the contrast or address both of them to further improve the single-photon switching efficiency. Here, we consider the physical limitations of the single-

photon switching phenomenon and offer ways to make it deterministic and operational at the level of a single shot simultaneously.

The intensity noise (or photon noise) of exciton-polariton BEC is a complex subject that depends on microscopic processes [15–18] as well as driven by many collective effects and multimode behaviour of the condensate [19–21] On the microscopic level the exciton component makes polariton Bose gas inherently nonlinear due to pair-particle repulsive interactions, that severely limits coherence [18, 22] and generates excessive intensity noise through the interaction with the incoherent excitonic reservoir [15–18, 23]. Alternatively, a large variety of different degrees of freedom in a solid-state leads to very sophisticated multimode dynamics of polariton BEC that may also be harnessed to control photon noise of the condensate [24]. Overall, the highly nonlinear behaviour of polariton condensates typically results in excessive intensity fluctuations well above the shot noise limit of an ideal coherent source.

Despite polariton BEC always exhibiting a super-Poisson noise, it also shows significant spatial and momentum disorder driven by dynamical instability [25–30] and inhomogeneous depletion of the reservoir (so-called hole burning effect) [30]. The actual mechanisms behind spatial-momentum disorder are still under debate. The physical origin of this instability comes from a nonequilibrium nature of polariton condensate, more specifically due to repulsive interaction between the condensate and reservoir when the last is not able to follow the condensate adiabatically (in the strongly nonadiabatic regime). On the contrary, the hole burning effect is due to spatially inhomogeneous reservoir depletion and acts as an effectively nonlinear attractive potential leading to self-focusing of polaritons in the condensate. The latter results in strong filamentation, spatial and momentum disorder. While extensively studied in theory such nontrivial spatial-momentum disorder is barely evidenced experimentally, pretty much because of the absence of single-shot measurements. To the best of our knowledge there are only few reports of the dynamical disorder observed in real space of single condensate realisations so far [28–30]. Our analysis of the single condensate realisation elucidates strong spatial and momentum disorder dynamically changing from shot to shot. Fig. S15 shows four consecutive single condensate realisations in a real space.

The strong fragmentation of the condensate in a real space inevitably impose disorder of the condensate density in momentum space. This disorder is a very important feature which actually defines intensity noise of the condensate in our measurements. It is worth to

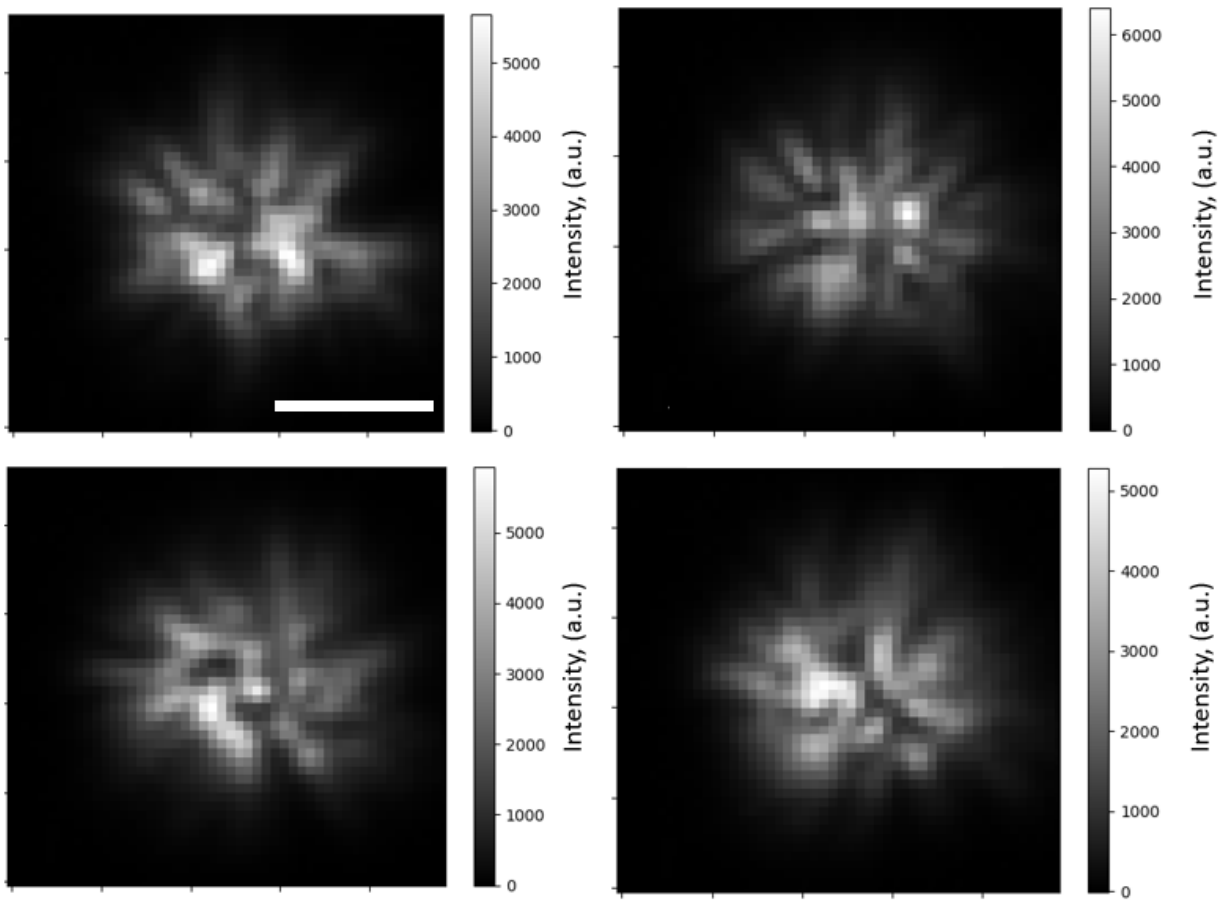

FIG. S15. Real-space distributions of emission from the system consecutively acquired in the single shot regime. The white bar scales the image to 20 μm.

mention that we applied a k-filter at the detection to increase the switching contrast, but at the same time it brings an extra noise on top of the intrinsic photon number fluctuation of the condensate. Indeed, due to its stochastic nature, the emission from the condensate can either pass through the k-filter (it leads to high intensity) or be filtered out (low intensity), depending on the density distribution in momentum space of the particular realization as shown in Fig. S16.

An alternative approach to reducing spatial disorder in our system is by utilising single/few mode cavities [31, 32]. Such structures suppress the reservoir instabilities and fluctuations that arise from the multi-mode nature of the flat Fabry-Pérot cavities. Moreover, the condensation dynamics is different from the cavities with continuous dispersion relation. Such change in cavity architecture will be extremely beneficial in terms of noise, (pump) energy efficiency.

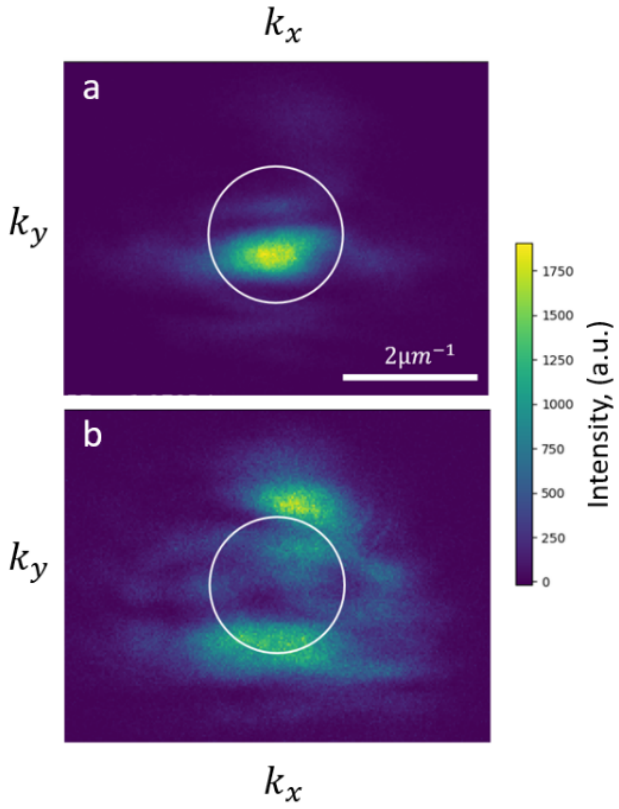

FIG. S16. Typical distributions of emission in momentum space

To quantify the lower limit of the noise in our particular system we collect large statistics of single condensate realisations without applying any k-filter and compare it with the data shown in Fig. 4e of the main text. Fig.S17 shows distributions of the total population of the spontaneously-formed condensate using k-filter (black solid line) and without it (dashed line) adopted by the number of counts and average value.

This comparison becomes crucial in understanding the origin of noise and the fundamental limits of the switching fidelity. It discriminates between the intrinsic noise of the condensate driven by underlying microscopic and collective nonlinear effects, and the noise attributed to the experimental arrangements and driven by the spatial-momentum disorder. The intrinsic noise of the condensate appears to be three times less than the noise of the single-photon switch at the same conditions and can be considered as the physical limit of the noise at the current arrangement. The fundamental limit of the condensate noise is much more difficult question to answer, especially in the case of Frenkel exciton-polariton systems. The complex nature of organic molecules and disordered character of their ensembles make theoretical studies of organic polariton condensates an extremely challenging task. From

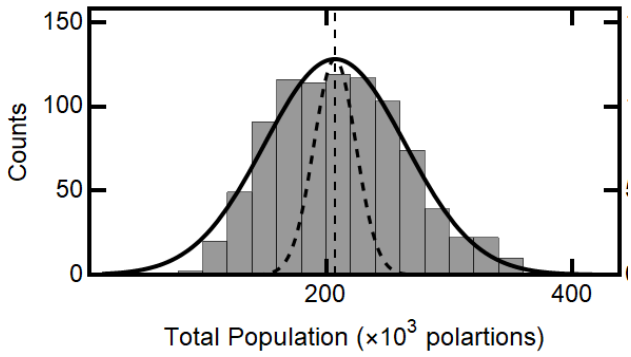

FIG. S17. Histogram of total polariton population of the spontaneously formed condensates (data from Fig. 4e of the main text). Black solid line is the Gaussian fit of the data. Black dashed line is the Gaussian fit of data obtained without k-filtering (adopted by the number of counts and average value).

an experimental point of view, a lack of reports in this regard also severely limits our understanding the noise. To explore the lowest boundary of the noise in our particular case we investigate fluctuations of the condensate in terms of total polariton population from shot-to-shot and calculate the time-integrated second-order coherence function $g^2(0) = 1 + \frac{\sigma^2 - \langle n \rangle}{\langle n \rangle^2}$, where σ and $\langle n \rangle$ are the standard deviation and mean value of the total polariton population distribution. Fig. S18 plots second-order coherence as a function of relative excitation density (P/P_{th}).

According to these data, the lowest shot noise limit ($g^2(0) = 1.002$) of the system is almost 6 times lower in standard deviation than the single photon switch noise shown in Fig. 4e of the main text ($g^2(0) = 1.08$). While it can be considered as the physical limitation of the noise in our system, it is still far from the fundamental limit of the shot noise $g^2(0) = 1$) that would lead to more than 2 orders of magnitude improvement in terms of standard deviation. Furthermore, the noise analysis and optimizations require comprehensive theoretical and experimental investigation of interconnections between microscopic and collective effects in the condensate with dynamical spatial-momentum disorder.

We believe the intrinsic noise of the condensate without k-filter is already at the promising level and further efforts should be paid to increase the contrast of single-photon switching. In fact, if we consider even the same experimental single-photon contrast of 11% but without using k-filter it would already provide a measurable enhancement in signal to noise ratio. To illustrate the idea, Fig. S19 plots total population of spontaneously-formed and seeded

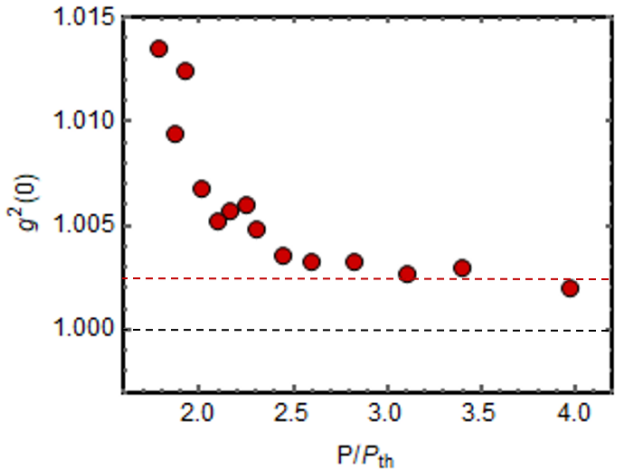

FIG. S18. Second-order coherence integrated over the condensate duration as a function of excitation density. The red dashed line shows the lower boundary of the system under investigation, while the black dashed line corresponds to an ideal coherent light source.

polariton condensates without k-flitter with 11% switching contrast.

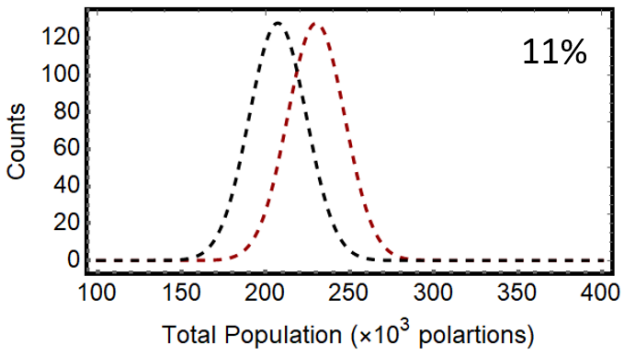

FIG. S19. Histograms of total population of spontaneously-formed and seeded polariton condensates adopted from the noise level (without k-filtering) and applying experimental contrast value of single-photon switching (11%).

The intuitive way to reduce the intrinsic noise due to quantum fluctuations and therefore improve switching contrast relies on suppression of polariton losses. Cavity photon lifetime and the effective exciton dephasing time are among the main factors limiting linewidth of polariton states. An increase the amount of layers at the distributed Bragg reflectors and improvement in quality of the structure is a straightforward route to suppress polariton losses in our system bearing high photonic fraction of the wave function of the ground state.

It is worth mentioning that the typical quality factors of organic microcavities are currently 100 1000, offering a huge room for technological improvements. We find that the maturity of inorganic systems is quite instructive in this regards; started out from Q-factor of 400 for the first strongly coupled GaAs-based microcavity reported in 1992 [33] it increased over three orders of magnitude by 2017 bringing polariton BEC to the level of thermal equilibrium [34]. Here we simulate single-photon switching contrast with k-filtering as a function of linewidth of seeded polariton states to see how much one could get from the particular material system with improved quality factor. Fig. S20 shows the contrast of the single-photon switching as a function of polariton linewidth.

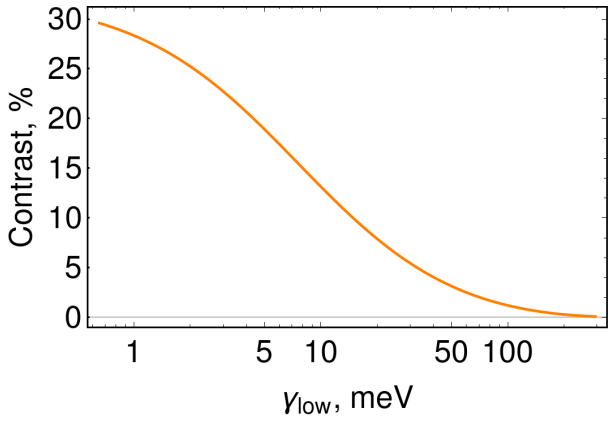

FIG. S20. Simulated contrast of the single-photon switching without k-filtering as a function of linewidth at the ground polariton state.

The linewidth of our system is about 10 meV according experimental data below condensation threshold as shown in Fig. S4b. This is a factor currently limiting the switching contrast to the level of 11%. However, one can achieve a measurable increase in contrast by further decreasing the linewidth. The current advancement in fabrication of strongly coupled organic microcavities enables the linewidth of 3 4 meV in half-wavelength cavities [1, 3, 7] which would double the contrast in our system and up to 200 eV in multi-wavelength structures [35] potentially corresponding to >30% single-photon contrast. To illustrate the result we plot histograms of total polariton population calculated for the linewidth below 1 meV. The distributions in Fig. S21 have been obtained assuming the noise level of spontaneously-formed condensate from experiments without using k-filter and 30% contrast of single-photon switching. The separation between the two distributions allows the switch states to be dis-

tinguished with 98.7% fidelity. Further contrast optimization is feasible albeit it requires in-depth theoretical and experimental study in a large parameter space of the system.

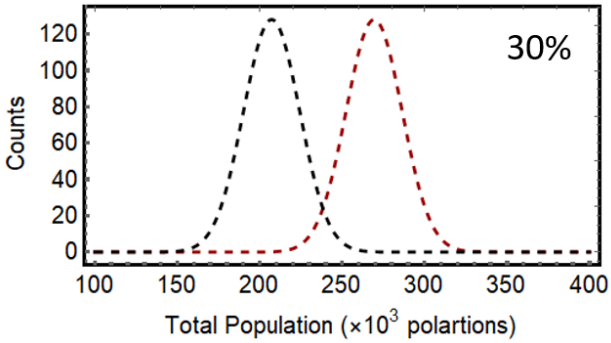

FIG. S21. Histograms of total population of spontaneously-formed and seeded polariton condensates adopted from the noise level (without k-filtering) and 30% contrast calculated for the system with improved linewidth $< 1\ meV$.

VII. PHOTON COUNTING OF SEED PULSES

In this section we provide the calibration data for the incident photon flux of the seed pulses based on a direct method of counting the seed photons transmitted through the sample. The seed beam is focused onto the sample within a wavevector range of $\pm 0.2 \mu\text{m}^{-1}$. The light transmitted through the sample is coupled to a single photon avalanche Si photodiode (SAPD) idq100 (ID Quantique) equipped with a 50 μm multi-mode fiber. To get rid of the noise we implement a time-gated photon counting scheme using a time-correlated single photon counting module SPC-160 (Becker & Hickel GmbH). We employ a standard inverse START-STOP technique to detect the photon events within 1 ns time window allowing for noise-free measurements. A photon detected on SAPD initiates the photon counting routine while the signal from the master laser terminates the measurement. We have carried out photon counting experiments at 500 Hz repetition rate applying five different seed energies that correspond to 2050, 143, 45, 12 and 3.5 photons per pulse on average, within the linewidth of the ground polariton state. Further on, we have quantified integrated photon detection efficiency (η), including transmittance of the sample (T), light coupling (K) and quantum efficiency (QE) of the SAPD: $\eta = T \cdot K \cdot QE \approx 0.01$. Fig. S22 shows an average photon count rate per seed pulse integrated over 60000 pulses (collection time of 120 s)

versus the average number of photons per pulse incident on the SAPD taking into account integrated detection efficiency η.

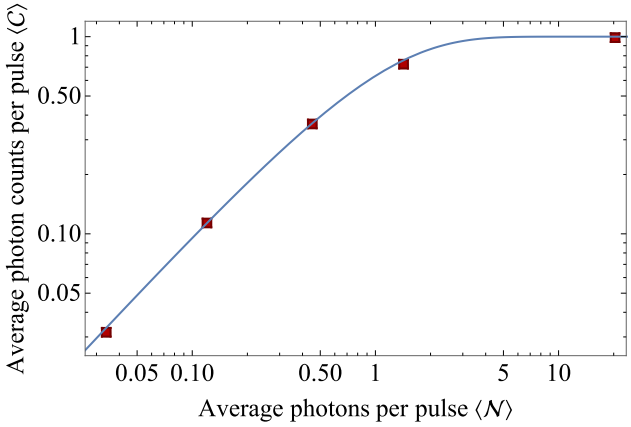

FIG. S22. The average photon counts per pulse $\langle C\rangle$ detected by the single photon counting setup within 120 s collection time as the function of the average photon numbers per seed pulse $\langle N\rangle$. The blue curve shows model values of $\langle C\rangle$ expected from theory for Poisson-distributed pulses, according the analytic expression $\sum_{m=1}^{\infty} \frac{\langle n\rangle^m e^{-\langle n\rangle}}{m!}$.

One can observe a clear linear dependence for the photon counts at the low incident photon numbers $\langle N\rangle \ll 1$ that saturates in the vicinity of $\langle N\rangle = 1$ with the maximum value of $\langle C\rangle$ equals 1 at $\langle N\rangle \gg 1$. The upper limit of $\langle C\rangle = 1$ relates to an operation principle of SAPD which generates a constant signal upon photon arrival regardless of the incident photon flux. The overall trend can be quantitatively explained in terms of summation over the probabilities to have at least one photon per seed pulse. Obeying Poisson distribution, the sum is defined as $\sum_{m=1}^{\infty} \frac{\langle n\rangle^m e^{-\langle n\rangle}}{m!}$. We plot the analytic expression in Figure S5 (blue curve). It reproduces our experimental observation in a very precise way which verifies our photon number calibration and serves as independent proof of the Poisson distribution of the seed beam.

[1] Plumhof, J. D., Stöferle, T. Mai, L., Scherf, U. & Mahrt, R. F. Room-temperature bose-einstein condensation of cavity exciton-polaritons in a polymer. *Nat. Mater.* **13**, 247-252 (2014).

[2] Zasedatelev, A.V. *et al.* A room-temperature organic polariton transistor. *Nat. Photon.* **13**, 378 (2019)

[3] Yagafarov, T. *et al.* Mechanisms of blueshifts in organic polariton condensates. *Communications Physics* **3**, 1–10 (2020).

[4] Grant, R.T. *et al.* Efficient radiative pumping of polaritons in a strongly coupled microcavity by a fluorescent molecular dye. *Advanced Optical Materials* **4**, 1615-1623 (2016).

[5] Rajendran, S.K. *et al.* Low Threshold Polariton Lasing from a Solution-Processed Organic Semiconductor in a Planar Microcavity. *Advanced Optical Materials* **7**, 1801791 (2019).

[6] Wei, M. *et al.* Room Temperature Polariton Lasing in Ladder-type Oligo(p-phenylene)s with Different -conjugation Lengths. *Advanced Photonics Research* (2020) https://doi.org/10.1002/adpr.202000044.

[7] Wei, M. *et al.* Low-threshold polariton lasing in a highly disordered conjugated polymer. *Optica* **6**, 1124–1129 (2019).

[8] Daskalakis, K.S., Majer, S.A., Murray, R.& Kéna-Cohen, S. Nonlinear interactions in an organic polariton condensate. *Nature Materials* **13**, 271–278 (2014).

[9] Kéna-Cohen, S. & Forrest, S.R. Room-temperature polariton lasing in an organic single-crystal microcavity. *Nature Photonics* **4**, 371–375 (2010).

[10] Somitsch, D *et al.* The Raman spectra of methyl substituted ladder type poly (p-phenylene): Theoretical and experimental investigations. *Synthetic Metals* **138**, 39–42 (2003).

[11] Born, M. & Oppenheimer, R Quantum Chemistry: Classic Scientific Papers. *World Scientific 20th Century Chemistry* **8**, 1–24 (2000).

[12] Carmichael, H. An open systems approach to quantum optics. *Springer-Verlag*, Berlin (1991).

[13] Scully, M.O., Zubairy, M.S. Quantum optics. *Cambridge University Press*, Cambridge (1997).

[14] Shishkov, V *et al.* Enhancement of the Raman Effect by Infrared Pumping. *Phys. Rev. Lett.* **122**, 153905 (2019).

[15] Deng, H *et al.* Condensation of Semiconductor Microcavity Exciton Polaritons. *Science* **298**,

199 (2002).

[16] Kasprzak, J *et al.* Second-order time correlations within a polariton Bose-Einstein condensate in a cdte microcavity. *Phys. Rev. Lett.* **100**, 067402 (2008).

[17] Love, A.P.D. *et al.* Intrinsic Decoherence Mechanisms in the Microcavity Polariton Condensate. *Phys. Rev. Lett.* **101**, 067404 (2008).

[18] Kim, S. *et al.* Coherent polariton laser. *Phys. Rev. X* **6**, 011026 (2016).

[19] Sala, V.G. *et al.* Stochastic precession of the polarization in a polariton laser. *Phys. Rev. B* **93**, 115313 (2016).

[20] Kusubo, K. *et al.* Stochastic formation of polariton condensates in two degenerate orbital states. *Phys. Rev. B* **87**, 214503 (2013).

[21] Whitaker, C.E. *et al.* Polariton Pattern Formation and Photon Statistics of the Associated Emission. *Phys. Rev. X* **7**, 031033 (2017).

[22] Askitopoulos, A. *et al.* Giant increase of temporal coherence in optically trapped polariton condensate. *Arxiv* **1911.08981**, (2019).

[23] Schmutzler, J. *et al.* Influence of interactions with noncondensed particles on the coherence of a one-dimensional polariton condensate. *Phys. Rev. B* **89**, 115119 (2014).

[24] Baryshev, S. *et al.* Engineering photon statistics in a spinor polariton condensate. *Arxiv* **2012.02774**, (2020).

[25] Bobrovska, N., Ostrovskaya, E. & Matuszewski, M. Stability and spatial coherence of nonresonantly pumped exciton-polariton condensates. *Phys. Rev. B* **90**, 205304 (2014).

[26] Bobrovska, N. & Matuszewski, M. Adiabatic approximation and fluctuations in exciton-polariton condensates. *Phys. Rev. B* **92**, 035311 (2015).

[27] Liew, T.C.H. *et al.* Instability-induced formation and nonequilibrium dynamics of phase defects in polariton condensates. *Phys. Rev. B* **91**, 085413 (2015).

[28] Daskalakis, K.S., Maier, S.A. & Kéna-Cohen, S. Spatial Coherence and Stability in a Disordered Organic Polariton Condensate. *Phys. Rev. Lett.* **115**, 035301 (2015).

[29] Bobrovska, N. *et al.* Dynamical Instability of a Nonequilibrium Exciton-Polariton Condensate. *ACS Photon.* **5**, 111 (2018).

[30] Estrecho, E. *et al.* Single-shot condensation of exciton polaritons and the hole burning effect. *Nat. Commun.* **9**, 2944 (2018).

[31] Urbonas, D. *et al.* Zero-Dimensional Organic ExcitonPolaritons in Tunable Coupled Gaussian

Defect Microcavities at Room Temperature. *ACS Photon.* **3**, 1542 (2016).

[32] Urbonas, D. *et al.* Room-Temperature Exciton-Polariton Condensation in a Tunable Zero-Dimensional Microcavity. *ACS Photon.* **5**, 85 (2018).

[33] Weisbuch, C., Nishioka, M., Ishikawa, A. & Arakawa, Y. Observation of the coupled exciton-photon mode splitting in a semiconductor quantum microcavity. *Phys. Rev. Lett.* **69**, 3314 (1992).

[34] Sun, Y. *et al.* Bose-Einstein Condensation of Long-Lifetime Polaritons in Thermal Equilibrium. *Phys. Rev. Lett.* **118**, 016602 (2017).

[35] Betzold, S. *et al.* Coherence and Interaction in confined room-temperature polariton condensates with Frenkel excitons. *ACS Photon.* **7,2**, 384 (2020).